Reducing self-interaction error in transition-metal oxides with different exact-exchange fractions for energy and density

Harshan Reddy Gopidi [1,2] Ruiqi Zhang,[3] Yanyong Wang [3] Abhirup Patra [4] Jianwei Sun [3] Adrienn Ruzsinszky [3] John P. Perdew [3,*] and Pieremanuele Canepa [1,2,†]

[1]*Department of Electrical and Computer Engineering, University of Houston, Houston, Texas 77204, USA*

[2]*Texas Center for Superconductivity, University of Houston, Houston, Texas 77204, USA*

[3]*Department of Physics and Engineering Physics, Tulane University, New Orleans, Louisiana 70118, USA*

[4]*Shell International Exploration and Production Incorporated, Houston, Texas 77082, USA*

(Received 3 December 2025; revised 8 March 2026; accepted 19 March 2026; published 10 April 2026)

Density functional theory (DFT) in chemistry and materials science aims for "chemical accuracy," but this goal is challenged by the need to approximate the exact exchange-correlation (XC) energy functional. The restored-regularized strongly constrained and appropriately normed (r^{2}SCAN), meta-generalized gradient approximation to the XC functional fulfills 17 exact constraints of the XC energy, and has significantly boosted prediction accuracy for molecules and materials. However, r^{2}SCAN remains inadequate at predicting the properties of open d and f transition-metal strongly correlated compounds, such as band gaps, magnetic moments, and oxidation energies. Prediction inaccuracies of r^{2}SCAN energies arise from functional- and density-driven errors, mainly resulting from the DFT self-interaction error. Here, we propose a method termed r^{2}SCANY@r^{2}SCANX to mitigate the self-interaction error of XC functionals for the accurate simulations of electronic, magnetic, and thermochemical properties of transition-metal oxides. r^{2}SCANY@r^{2}SCANX uses different fractions of exact Hartree-Fock exchange, X for the electronic density and Y for the density functional approximation of the total energy, thereby simultaneously addressing functional-driven and density-driven inaccuracies. Building on just one (or maximum two) parameters that apply unchanged to *s-p*-bonded systems, we demonstrate that r^{2}SCANY@r^{2}SCANX improves upon the r^{2}SCAN predictions for 20 highly correlated oxides and even outperforms the highly parametrized DFT(r^{2}SCAN)+U method—the state-of-the-art approach to predict strongly correlated materials. Prediction uncertainties for oxidation energies and magnetic moments of transition-metal oxides are significantly reduced by r^{2}SCAN10@r^{2}SCAN50 and band gaps with r^{2}SCAN10@r^{2}SCAN. r^{2}SCAN10@r^{2}SCAN50 diminishes the density-driven error of the energy in r^{2}SCAN and r^{2}SCAN10. We demonstrate that the computationally efficient r^{2}SCAN10@r^{2}SCAN is nearly as accurate as the global hybrid r^{2}SCAN10 for oxidation energies. This indicates that accurate energy differences can be obtained through rate-limiting self-consistent iterations and geometry optimizations with the efficient r^{2}SCAN. Subsequently, a more expensive nonlocal functional, such as a hybrid or self-interaction correction, can be applied in a fast, single post-self-consistent calculation, as in r^{2}SCAN10@r^{2}SCAN.

DOI: 10.1103/myd5-l4f4

I. INTRODUCTION

Electronic structure methods, especially density functional theory (DFT) [1], have become essential for materials discovery, enabling the prediction of properties and behaviors of technologically relevant materials [2–6]. This has resulted in the widespread use of DFT for extensive materials databases, such as the Alexandria Materials Database [7], AFLOW [8], GNoME [9], the Materials Project [3], the NREL materials databases [10], and OQMD [2]. These databases provide a critical foundation for materials science research, enabling direct comparison of computed properties with experimental data, developing predictive models, and lately, foundational training sets for machine learning potentials [11–14], thus necessitating highly accurate datasets approaching "chemical accuracy."

Nevertheless, DFT in the Kohn-Sham formulation requires approximations for the exact exchange and correlation (XC) functional, which has been a matter of intense research for the past 60 years [15–17]. Among the density functional approximations (DFAs), the local spin density approximation (LSDA) [1,18], and the generalized gradient approximation (GGA) [19] exhibit inaccuracies in predicting structural parameters, energetics, and electronic properties, especially for strongly correlated systems. DFA and XC are synonyms and will be used interchangeably.

The strongly constrained and appropriately normed approximation (SCAN) [20] and its regularized and computationally efficient version r^{2}SCAN [21] are highly accurate meta-GGA functionals. SCAN and r^{2}SCAN satisfy 17 known exact constraints for constructing XC functionals, ensuring a well-balanced description of XC effects for a wide range of

*Contact author: perdew@tulane.edu

†Contact author: pcanepa@uh.edu

systems [22]. The LAK (Lebeda-Aschebrock-Kümmel) approximation is a constraint-based meta-GGA that accurately describes electronic bonding and band gaps of main-group molecules and semiconductors [23]. SCAN and r^{2}SCAN have done admirably well in improving the quality of predictions of molecules and materials relative to GGA [24–29]. Most materials databases depend on GGA's predictive power, using *ad hoc* corrections, e.g., GGA+U [10,30,31], or newer DFA, e.g., r^{2}SCAN [32].

Challenges persist when SCAN and r^{2}SCAN are used to predict several valuable material properties of open d (f) transition-metal compounds, including band gaps, magnetic moments, and oxidation (reduction) energies. While r^{2}SCAN (SCAN) reduces the self-interaction error (SIE) magnitude compared to standard semilocal GGA XC functionals, this pernicious error remains [21,24,25,33–37].

Pragmatic but material- and property-dependent solutions to address the SIE in GGAs and meta-GGAs involve parametrizing *ad hoc* on-site Hubbard U corrections, such as GGA(LSDA)+U [38], and r^{2}SCAN(SCAN)+U [26–28,30,31,39–41]. Although numerically accurate and affordable, these +U approaches often lack transferability because the U parameters depend on material chemistry, dimensionality, and the oxidation states of transition metals. Strategies exist to fit the U values to the thermochemical data of redox reactions [26–28,30,31,40,41], or band gaps [38,42]. U values can also be derived from linear response [43,44], or with machine learning models [45,46]. A persistent issue is that applying a U-specific value to oxidation energies does not ensure the same U will accurately replicate band gaps or magnetic moments in similar materials [30,31].

Hybrid XC functionals are a universal approach to address SIE in materials [47–59], replacing part of the DFA exchange with a fraction of exact Hartree-Fock (HF) exchange. Global and range-separated hybrids are successfully applied to transition-metal oxides (M_iO_j's) [47–65].

Although most hybrid functionals have a preset HF exchange parameter [66,67], they are less sensitive to material types or specific reactions and properties [47–65,68]. A few nonempirical methods exist to estimate HF exchange [64,69–76]. This paper explores several global r^{2}SCAN-based hybrid functionals with X% of exact HF exchange, termed r^{2}SCANX.

Building on the idea that HF provides self-interaction-free, uncorrelated densities, an elegant solution is to use HF electronic charge densities to compute r^{2}SCAN total energies [77–83]. This approach is called the Hartree-Fock density functional theory or DFA@HF [83], and has been successfully applied to molecules [77–83]. In almost all cases, r^{2}SCAN@HF is significantly more accurate or slightly less accurate than SCAN/r^{2}SCAN [83,84]. There are instances where HF densities are more accurate than those of specific XC functionals when describing molecular systems, especially charge-transfer reactions. In other cases, an "unconventional error cancellation" discussed in Refs. [83,85,86] occurs, leading to surprisingly good numerical results, even when HF electronic densities are less accurate than r^{2}SCAN densities. This paper proposes an r^{2}SCAN@HF-like approach to predict the electronic and magnetic properties of open-d first row transition-metal oxides and their oxidation reactions, avoiding the unconventional error cancellation which we show does not occur in these transition-metal oxides.

Unconventional error cancellations observed in r^{2}SCAN@HF is demonstrated in Eq. (1) [87–90], expressing the error of the DFT total energy E as a sum of a functional-driven error, FE, intrinsic to the DFA, and a density-driven error, DE, caused by inaccuracies carried by the DFA electron density n,

$$\begin{aligned}\Delta E_{\mathrm{DFA}} &= E_{\mathrm{DFA}}[n_{\mathrm{DFA}}] - E_{\mathrm{exact}}[n_{\mathrm{exact}}] = \mathrm{FE} + \mathrm{DE},\\ \mathrm{FE} &= E_{\mathrm{DFA}}[n_{\mathrm{exact}}] - E_{\mathrm{exact}}[n_{\mathrm{exact}}],\\ \mathrm{DE} &= E_{\mathrm{DFA}}[n_{\mathrm{DFA}}] - E_{\mathrm{DFA}}[n_{\mathrm{exact}}],\end{aligned} \tag{1}$$

where n_{DFA} is the "inaccurate" charge density provided by the DFA, and n_{exact} is the unknown exact density. To evaluate FE and DE of Eq. (1), an exact (or nearly exact) electron density is needed. References [83,85,86] used the coupled cluster single-double and perturbative triple excitations [CCSD(T)] density, which is nearly exact in typical *sp*-bonded systems, and found that, for those systems, it produced FE and DE values very close to using the r^{2}SCAN50 (the global hybrid of r^{2}SCAN with 50% of HF exchange) density as the exact density. Then r^{2}SCAN50 was used as the proxy for the exact density in all such systems [83,85,86]. The r^{2}SCAN50 density was understood to provide correct electron transfers [91] from one atomic site to another, a feature of the electron density to which the total energy appears especially sensitive. Increasing the exact-exchange fraction X is expected [92] to increase the tendency to put an integer number of electrons on each species. Our experience with self-consistent DFAs shows that DE is generally much smaller than FE for transition-metal oxidation energies, main-group barrier heights, and water binding energies in clusters [83,85,93]. DE is dominated by electron transfer errors, and insensitive to other density errors [83].

In *sp*-bonded systems with minimal or no electron transfer, the r^{2}SCAN densities were more accurate than HF densities [94,95]. The improvement in density from HF to LSDA, to Perdew-Burke-Ernzerhof (PBE), and to r^{2}SCAN shows the predictive power of including systematically more exact constraints in the DFA [22,85,86]. References [22,85,86] concluded that DFA@HF, in which a DFA is evaluated on the HF orbitals and densities, often works through an unconventional error cancellation between the FE of the DFA and the DE of the HF density, $E_{\mathrm{DFA}}[n_{\mathrm{HF}}]$-$E_{\mathrm{DFA}}[n_{\mathrm{exact}}]$ (called the nonvariational density overlocalization in Ref. [86]). For example, Ref. [83] found that unconventional error cancellation improved barrier heights in molecular reactions, mainly affected by SIE. This observation has been linked to error cancellation between large negative values of FE [Eq. (1)] counterbalanced by correspondingly large positive values of DE, the latter caused by uncorrelated and overlocalized HF charge densities [83].

We show that DFA@HF fails for transition-metal oxides due to insufficient error cancellation. Therefore, more accurate methodologies for the SIE in transition-metal oxides are introduced. By independently correcting FE and DE [Eq. (1)], we address the SIE of the XC functional in predicting electronic, magnetic, and thermodynamic properties. This is achieved by mixing different fractions of exact HF exchange into the DFA used to evaluate the total energy

and compute the electronic charge density. This strategy is applied with the previously proposed r^{2}SCAN, resulting in a generalized r^{2}SCANY@r^{2}SCANX approach, where Y is the percentage of exact HF exchange mixed with the r^{2}SCAN functional used to evaluate energy. X represents the % of exact HF exchange mixed with r^{2}SCAN used to compute the orbitals and, hence, the electronic charge density.

We will show that when r^{2}SCANY@r^{2}SCANX is applied to transition-metal oxides' oxidation energies, as values of Y and/or X increase, the error in oxidation energies drops noticeably minimizing at Y $\sim$ 10% and X $\sim$ 50%. Importantly, these values for the transition-metal oxides are those we expected, based on experience with *s*-*p*-bonded systems: Since r^{2}SCAN has less self-interaction error than PBE, its non-negligible functional-driven error of the energy can be reduced by using 10% of HF exchange, less than the 25% that PBE needs. Since the smaller density-driven error of the energy is dominated by electron-transfer error, the density and orbitals need 50% of HF exchange to reduce these delocalization errors.

We will further propose a computationally efficient, non-self-consistent, r^{2}SCAN10@r^{2}SCAN approach that significantly improves the accuracy of oxidation energies compared to r^{2}SCAN and is on par with highly parametrized r^{2}SCAN + U approaches. We will also demonstrate that r^{2}SCAN10@r^{2}SCAN outperforms r^{2}SCAN and r^{2}SCAN + U in accuracy for band gaps.

II. RESULTS

A. Improving *ab initio* predictions of meta-GGA-type r^{2}SCAN functionals

All XC functionals suffer from functional-driven and density-driven errors [Eq. (1)]. SIE, a significant part of both errors, leads to inaccurate predictions of energetics in molecules and materials. LSDA, GGA, and meta-GGA XC functionals struggle to accurately describe properties, such as reaction energies, interatomic charge transfer, and electronic structure in systems with strongly localized open-shell d (or f) electrons, as in M_iO_j's [10,26,27,30,31,38–40,96–100].

To address the SIE, we present the generalized r^{2}SCANY@r^{2}SCANX approach, which builds upon r^{2}SCAN. In r^{2}SCANY@r^{2}SCANX, the SIE is addressed by independently tuning the fraction of exact HF exchange directly in the r^{2}SCAN hybrid functional definition used to evaluate the total energy of a given set of orbitals and the r^{2}SCAN hybrid functional used to compute these orbitals. In r^{2}SCANY@r^{2}SCANX, Y is the percent of HF exact exchange appearing in the XC energy of r^{2}SCAN to correct the functional-driven error. In contrast, in r^{2}SCANY@r^{2}SCANX, X is the percentage of HF exchange used in the r^{2}SCAN functional to determine the electronic orbitals and potentially correct for the density-driven error. By independently varying the X% and Y% parameters in r^{2}SCANY@r^{2}SCANX, the proposed method enables a more systematic correction of the functional- and density-driven errors inherent in r^{2}SCAN's formulation, with the aim of improving the accuracy in describing transition-metal oxides and potentially other correlated systems.

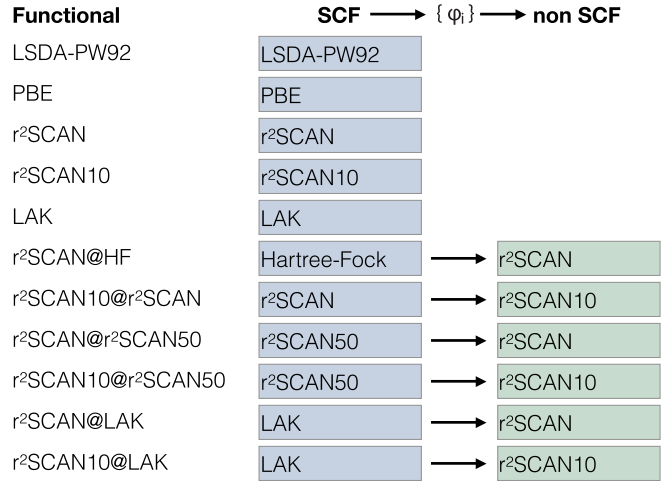

FIG. 1. Schematically connecting the self-consistent and non-self-consistent (non-SCF) approaches required in the r^{2}SCANY@r^{2}SCANX methods. The self-consistent functionals used in this work are LSDA, PBE, r^{2}SCAN, r^{2}SCAN10, and LAK. The non-self-consistent hybrid functionals, including a fraction of exact HF exchange, such as r^{2}SCAN@HF, r^{2}SCAN10@r^{2}SCAN, r^{2}SCAN@r^{2}SCAN50, r^{2}SCAN10@r^{2}SCAN50, r^{2}SCAN@LAK, r^{2}SCAN10@LAK, require a self-consistent step to generate orbitals on which the energy is evaluated non-self-consistently.

In r^{2}SCANY@r^{2}SCANX, the XC energy functional ($E_{xc} = E_{xc}^{Y}[n^X]$) is defined as

$$E_{xc}^{Y}[n^X] = \frac{Y}{100}E_x^{HF}[n^X] + \left(1 - \frac{Y}{100}\right)E_x^{r^2SCAN}[n^X] + E_c^{r^2SCAN}[n^X], \quad (2)$$

where, in Eq. (2), n^X is the self-consistent electron density from the r^{2}SCAN energy functional, including X% of HF exchange. Therefore, the r^{2}SCANY@r^{2}SCANX definition incorporates different fractions of exact exchange in the energy and self-consistent electron density, ensuring a more systematic correction of SIE. Replacing a small fraction of r^{2}SCAN exchange with the same fraction of HF exchange should have minimal or no effect on satisfying the exact DFT constraints of r^{2}SCAN.

Using Eq. (2) and specific X and Y values, we propose different r^{2}SCANY@r^{2}SCANX XC functionals (Fig. 1). The approach of Eq. (2) is not self-consistent unless Y = X. Figu re 1 lists in its second column (SCF) DFAs of interest here that can be implemented self-consistently to find orbitals, a density, and a total energy. The third column (non-SCF) in Fig. 1 lists functionals that could be evaluated on those orbitals and that density to find a possibly better total energy. In the SCF part, functionals LDSA-PW92 [18], the GGA PBE [19], the meta-GGAs r^{2}SCAN [20,101] (plain or hybrid), or LAK were used [23].

B. r^{2}SCAN predictions of transition-metal oxide properties

Here, we consider a diverse group of binary transition-metal oxides of the type M_iO_j. M is a first row transition metal Ti, V, Cr, Mn, Fe, Co, Ni, Cu, and Zn with a

closed- or open-shell electronic structure. The predicted energetics of these compounds are then used to compute the oxidation energies of M_iO_j's oxidation reactions. The M_iO_j's comprise the following: TiO_2 ($P4_2/mnm$) [102], Ti_2O_3 ($R\bar{3}c$) [103], VO ($Fm\bar{3}m$) [104], V_2O_3 ($I2/a$) [105], VO_2 ($P2_1/c$) [106], V_2O_5 ($Pmmn$) [107], Cr_2O_3 ($R\bar{3}c$) [108], CrO_3 ($C2cm$) [109], CrO_2 ($P4_2/mnm$) [110], MnO ($Fm\bar{3}m$) [111], MnO_2($P4_2/mnm$) [112], Mn_3O_4 ($I4_1/amd$) [113], Fe_2O_3 ($R\bar{3}c$) [114], FeO ($Fm\bar{3}m$) [115], Fe_3O_4 ($Fd\bar{3}m$) [116], CoO ($Fm\bar{3}m$) [111], Co_3O_4 ($Fd\bar{3}m$) [117], NiO ($Fm\bar{3}m$) [118], CuO ($C2/c$) [119], Cu_2O ($Pn\bar{3}m$) [120], and ZnO ($P6_3mc$) [121]. These M_iO_j's were selected based on the availability of reliable experimental formation enthalpies, good structural reports sourced from the Inorganic Crystal Structure Database (ICSD) [122], and M_iO_j ground-state magnetic orderings, whenever required.

Table I summarizes the experimental and predicted lattice parameters, magnetic moments, and band gaps of all materials using r^{2}SCAN and r^{2}SCAN + U (with U values from Ref. [40]). Data reported in Table I used r^{2}SCAN geometry-optimized structures, including the relaxation of atomic positions, volumes, and cell shapes. For the r^{2}SCAN + U dataset, this functional was used for geometry optimization (atomic positions, volumes, and shapes). Further, we tested M_iO_j's oxidation energies and their electronic properties for a fixed $U = 2$ eV on transition metals.

Previous studies have shown that r^{2}SCAN (SCAN) geometries agree well with experimental data [24,26,27,39,40]. Data in Table I confirm the accuracy of r^{2}SCAN in predicting the lattice parameters and magnetic configurations of M_iO_j's and are consistent with Ref. [40]. Exceptions to this trend are VO (∼8.9%) and CuO (∼14%), whose lattice constants deviate from experimental reports [104,119].

Mn_3O_4 is known to exhibit complex magnetism [123], which was approximated by setting a collinear magnetic configuration that best approximates the experimentally observed magnetic ground state. Ti_2O_3 is diamagnetic upon dimerization [124], and modeled as nonmagnetic here. VO_2 also dimerizes, which is described with an antiferromagnetic configuration [125]. These choices of magnetic configurations in Ti_2O_3 and VO_2 are based on the best approach proposed here (r^{2}SCAN10@r^{2}SCAN50) (see Supplemental Fig. 1 [126]). For many of the nonmagnetic materials in Table I (TiO_2, V_2O_5, CrO_3, Cu_2O, and ZnO), the assumption that each oxygen is a closed-shell O^{2-} anion leaves no valence electron on the transition-metal cation.

Experimentally, Ti_2O_3 (∼0.2 eV), V_2O_3 (∼0.2 eV), and Fe_3O_4 (∼0.14 eV) have small experimental band gaps, respectively, but are predicted to be metallic with r^{2}SCAN and consistent with previous results in Ref. [40].

C. Benchmarking oxidation enthalpies of M_iO_j's with r^{2}SCANY@r^{2}SCANX functionals

The XC functionals of Fig. 1 were used to assess the oxidation enthalpies of several M_iO_j's (M = Ti, V, Cr, Mn, Fe, Co, and Cu) as defined for $z > x$ in Eq. (3):

$$\frac{2}{z-x}MO_x + O_2 \rightarrow \frac{2}{z-x}MO_z. \tag{3}$$

Following Eq. (3), and using various r^{2}SCANY@r^{2}SCANX DFAs, we computed all possible oxidation enthalpy reactions using the M_iO_j's in Table I and Eq. (4), resulting in 18 distinct reactions summarized in Table II. The negative chemical energy change in the reaction is

$$\begin{aligned}\Delta H_0 = &\frac{2}{z-x}E(MO_z)^{\text{r}^2\text{SCANY@r}^2\text{SCANX}}\\ &-\frac{2}{z-x}E(MO_x)^{\text{r}^2\text{SCANY@r}^2\text{SCANX}}\\ &-E(O_2)^{\text{r}^2\text{SCANY@r}^2\text{SCANX}},\end{aligned} \tag{4}$$

where $E(MO_z)^{\text{r}^2\text{SCANY@r}^2\text{SCANX}}$, $E(MO_x)^{\text{r}^2\text{SCANY@r}^2\text{SCANX}}$, $E(O_2)^{\text{r}^2\text{SCANY@r}^2\text{SCANX}}$, are the r^{2}SCANY@r^{2}SCANX total energies of the oxidized, reduced M_iO_j's, and O_2 gas, respectively. Our DFT predictions are compared to experimental oxidation reaction enthalpies shown in Table II, obtained from the formation energies of MO_x and MO_z (Supplemental Table 2 [126]) extracted from experimental reports [127,128]. Thermochemical tables provide oxidation energies with an uncertainty range that should include the true value 95% of the time. Furthermore, the definition of the bounds of the mean absolute error used in theoretical work is narrower than the typical standard deviation set to a 95% level of confidence imposed in thermochemical tables. In addition, here we approximated the oxidation enthalpies by the DFT total energies by imposing $\Delta H_0 \approx \Delta E$, thus neglecting the pressure-volume contributions, which are expected to be minimal.

Figure 2 displays the deviation of predicted oxidation enthalpies including common XC functionals, such as LSDA [18], PBE [19], and meta-GGA, including r^{2}SCAN [101] and LAK [23], as well as r^{2}SCANY@r^{2}SCANX (r^{2}SCANY@LAK) derivatives. From the benchmarking of 18 predicted oxidation energies with experimental values, we derived the error distributions in Fig. 2(b), and the mean absolute errors (MAEs) of Fig. 2(c). Note, errors in oxidation energies with all methods were evaluated using r^{2}SCAN geometries. For the r^{2}SCAN + U dataset, the M_iO_j's geometries were optimized using r^{2}SCAN + U.

As shown in Figs. 2(b) and 2(c), the errors in predicting oxidation energies for M_iO_j's with LSDA, PBE, and r^{2}SCAN reduce systematically as the quality of the exchange-correlation functional increases from LSDA to PBE, and to meta-GGA. In this sequence, the number of exact constraints on the exchange-correlation energy that can be satisfied increases from 8 to 11 to 17. Predictions with these XC functionals are affected to different extents by the SIE [16]. Therefore, we will focus on r^{2}SCAN and its hybrids r^{2}SCANY@r^{2}SCANX (Fig. 1).

In Fig. 2(c), r^{2}SCAN exhibits a mean absolute error (MAE) of ∼1.09 eV/O_2 and a root mean squared error (RMSE) of ∼1.29 eV/O_2 in oxidation enthalpies in our dataset. r^{2}SCAN systematically makes oxidation energies too negative across all tested cases. This is largely a functional-driven error.

The r^{2}SCAN + U implemented here used U parameters from Ref. [40]. We have also tested r^{2}SCAN + U calculations, with U fixed to 2 eV. When applied to the 18 oxidation reactions (excluding the one for Ce), r^{2}SCAN + U yields a milder deviation from experimental data, with an MAE of

TABLE I. r^{2}SCAN and r^{2}SCAN+U (with U values from Ref. [40]) predicted lattice parameters, on-site magnetic moments (in μ_B), and band gaps (in eV) of M_iO_j's. Experimental quantities are marked as Expt. Unless mentioned, all calculations use experimentally determined magnetic orderings (M.O.), referenced in the magnetic moment (M.M.) column. Antiferromagnetic (AFM), ferrimagnetic (FEM), ferromagnetic (FM), diamagnetic-via-dimerization (DM−d), and nonmagnetic orderings (NM) are indicated. Spin-polarized calculations were used for all FM, AFM, and FEM systems, while NM materials were treated with spin-restricted calculations. See Supplemental Table 1 for U values used in Supplemental Material [126].

System	Method	a	b	c	α	β	γ	M.M.	M.O.	Band Gap
	Expt.	4.59	4.59	2.96	90	90	90	0.00	NM	3.0 [129]
TiO_2 ($P4_2/mnm$) [102]	r^{2}SCAN	4.60	4.60	2.96	90	90	90	0.00	NM	2.24
	r^{2}SCAN+U	4.62	4.62	2.99	90	90	90	0.00	NM	2.51
	Expt.	5.43	5.43	5.43	56.57	56.57	56.57	$\leqslant$0.03 [124]	DM−d	0.20 [130]
Ti_2O_3 ($R\bar{3}c$) [103]	r^{2}SCAN	5.46	5.46	5.46	57.76	57.76	55.76	0.00	NM	0.00
	r^{2}SCAN+U	5.42	5.42	5.42	57.53	57.53	57.53	0.00	NM	0.59
	Expt.	2.88	2.88	4.99	73.22	90	120	N/A	AFM	N/A
VO ($Fm\bar{3}m$) [104]	r^{2}SCAN	3.16	3.16	4.89	71.12	90	120	2.45	AFM	1.66
	r^{2}SCAN+U	3.16	3.16	5.00	71.54	90	119.99	2.55	AFM	2.35
	Expt.	7.25	5.00	5.55	90	96.75	90	1.2/2.37 [131,132]	AFM	0.20 [133]
V_2O_3 ($I2/a$) [105]	r^{2}SCAN	7.28	5.00	5.51	90	97.50	90	1.70	AFM	0.00
	r^{2}SCAN+U	7.28	5.08	5.56	90	96.42	90	1.80	AFM	0.68
	Expt.	5.75	4.53	5.38	90	122.69	90	0.00 [134]	DM−d	0.70 [133]
VO_2 ($P2_1/c$) [106]	r^{2}SCAN	5.88	4.49	5.35	90	123.21	90	0.93	AFM	0.17
	r^{2}SCAN+U	5.94	4.46	5.37	90	123.65	90	0.98	AFM	0.69
	Expt.	11.51	3.56	4.37	90	90	90	0.00	NM	2.5 [135]
V_2O_5 ($Pmmn$) [107]	r^{2}SCAN	11.59	3.55	4.25	90	90	90	0.00	NM	2.04
	r^{2}SCAN+U	11.59	3.56	4.25	90	90	90	0.00	NM	2.14
Cr_2O_3 ($R\bar{3}c$) [108]	Expt.	4.95	4.95	13.60	90	90	120	2.76 [136]	AFM	3.2 [137]
	r^{2}SCAN	4.94	4.94	13.62	90	90	120	2.58	AFM	2.58
CrO_3 ($C2cm$) [109]	Expt.	4.79	8.56	5.74	90	90	90	0.00	NM	3.8 [138]
	r^{2}SCAN	4.86	8.25	5.70	90	90	87.91	0.00	NM	2.30
CrO_2 ($P4_2/mnm$) [110]	Expt.	4.42	4.42	2.92	90	90	90	2.00 [139]	FM	0.00 [139]
	r^{2}SCAN	4.40	4.40	2.91	90	90	90	2.06	FM	0.00
	Expt.	3.14	3.14	6.29	60	60	60	4.58 [140]	AFM	3.6/3.8 [141]
MnO ($Fm\bar{3}m$) [111]	r^{2}SCAN	3.14	3.14	6.17	59.36	59.36	59.98	4.30	AFM	1.74
	r^{2}SCAN+U	3.15	3.15	6.21	59.50	59.50	59.99	4.42	AFM	2.13
	Expt.	4.40	4.40	2.87	90	90	90	2.35 [142]	AFM	0.27/0.3 [143,144]
MnO_2 ($P4_2/mnm$) [112]	r^{2}SCAN	4.38	4.38	2.86	90	90	90	2.62	AFM	0.39
	r^{2}SCAN+U	4.39	4.39	2.88	90	90	90	2.77	AFM	0.74
	Expt.	5.76	5.76	6.24	117.52	117.52	90	4.34, 3.25/3.6 [123]	FEM	2.3–2.5 [145]
Mn_3O_4 ($I4_1/amd$) [113]	r^{2}SCAN	5.72	5.72	6.22	117.39	117.39	90	4.19, 3.51	FEM	0.96
	r^{2}SCAN+U	5.76	5.76	6.24	117.50	117.50	90	4.36, 3.64	FEM	1.39
	Expt.	6.08	6.08	6.08	60	60	60	3.32/4.2 [146,147]	AFM	2.20 [148]
FeO ($Fm\bar{3}m$) [115]	r^{2}SCAN	5.87	6.13	5.96	62.31	60.48	61.39	3.42	AFM	0.43
	r^{2}SCAN+U	6.11	6.10	6.10	61.04	59.91	59.95	3.54	AFM	1.58
	Expt.	5.03	5.03	13.76	90	90	120	4.9 [149]	AFM	2.20 [150]
Fe_2O_3 ($R\bar{3}c$) [114]	r^{2}SCAN	5.00	5.00	13.74	90	90	120	3.86	AFM	1.52
	r^{2}SCAN+U	5.04	5.04	13.75	90	90	120	4.12	AFM	1.50
	Expt.	8.39	8.39	8.39	90	90	90	4.44, 4.1 [116]	FEM	0.14 [151]
Fe_3O_4 ($Fd\bar{3}m$) [116]	r^{2}SCAN	8.34	8.34	8.34	90	90	90	3.73; 3.70	FEM	0.00
	r^{2}SCAN+U	8.44	8.47	8.37	90.01	90.28	90.03	4.12; 3.58	FEM	0.23
	Expt.	3.01	3.01	6.03	60	60	60	3.35/3.8 [146,152]	AFM	2.40 [153,154]
CoO ($Fm\bar{3}m$) [111]	r^{2}SCAN	2.99	2.99	5.96	59.92	59.92	60	2.54	AFM	0.85
	r^{2}SCAN+U	3.01	3.01	5.97	59.78	59.78	60	2.62	AFM	2.12
	Expt.	8.07	8.07	8.07	90	90	90	3.02 [155]	AFM	1.60 [154]
Co_3O_4 ($Fd\bar{3}m$) [117]	r^{2}SCAN	8.03	8.03	8.03	90	90	90	2.45	AFM	1.12
	r^{2}SCAN+U	8.06	8.06	8.06	90	90	90	2.57	AFM	1.94

TABLE I. *(Continued.)*

System	Method	a	b	c	α	β	γ	M.M.	M.O.	Band Gap
	Expt.	2.93	2.93	5.87	60	60	60	1.64/1.90 [98,140]	AFM	4.3 [96]
NiO ($Fm\bar{3}m$) [118]	r^{2}SCAN	2.94	2.94	5.88	59.91	59.91	60.07	1.59	AFM	2.42
	r^{2}SCAN+U	2.95	2.95	5.90	59.97	59.97	60.03	1.69	AFM	3.52
CuO ($C2/c$) [119]	Expt.	6.32	3.42	7.50	90	95.23	90	0.68 [156]	AFM	1.40 [157]
	r^{2}SCAN	6.35	3.90	6.95	90	100.89	90	0.56	AFM	0.69
Cu$_2$O ($Pn\bar{3}m$) [120]	Expt.	4.27	4.27	4.27	90	90	90	0.00	NM	2.17/2.4 [25,157]
	r^{2}SCAN	4.24	4.24	4.24	90	90	90	0.00	NM	2.20
ZnO ($P6_3mc$) [121]	Expt.	3.25	3.25	5.21	90	90	120	0.00	NM	3.4 [158]
	r^{2}SCAN	3.24	3.24	5.20	90	90	119.99	0.00	NM	1.25
	Expt.	5.41	5.41	5.41	90	90	90	0.00	NM	3.32 [159]
CeO$_2$ ($Fm\bar{3}m$) [160]	r^{2}SCAN	5.44	5.44	5.44	90	90	90	0.00	NM	2.20
	r^{2}SCAN+U	5.45	5.45	5.45	90	90	90	0.00	NM	2.35
	Expt.	3.89	3.89	6.06	90	90	120	1.08 [161]	AFM	2.34 [159,162]
Ce$_2$O$_3$ ($P\bar{3}m$) [163]	r^{2}SCAN	3.87	3.87	6.05	90	89.99	120	0.94	AFM	0.57
	r^{2}SCAN+U	3.89	3.89	6.09	90	90	120	0.97	AFM	1.90

$\sim$0.57 eV/O$_2$ and an RMSE of $\sim$0.70 eV/O$_2$. As expected, setting a standard $U = 2$ eV for all transition metals worsens the MAE to $\sim$0.78 eV/O$_2$ and an RMSE to $\sim$0.92 eV/O$_2$.

A self-consistent global hybrid, such as r^{2}SCAN10, incorporating 10% of exact HF exchange should partly mitigate the SIE inaccuracies of the r^{2}SCAN meta-GGA, but at the expense of slightly higher computational costs than for GGA-based global hybrids (and considerably higher than the cost of pure meta-GGAs). As expected, the r^{2}SCAN10 functional significantly reduces the errors, yielding an MAE of $\sim$0.66 eV/O$_2$ and an RMSE of $\sim$0.73 eV/O$_2$ (Fig. 2). This represents approximately a 40% reduction in errors compared to r^{2}SCAN.

When applying r^{2}SCAN@HF and using the HF electronic density for the r^{2}SCAN total energy evaluation, the MAE for our dataset is 1.59 eV/O$_2$ and an RMSE of 1.92 eV/O$_2$. This indicates a decline of approximately 45% in accuracy compared to standard r^{2}SCAN. Similarly to r^{2}SCAN@HF, one can reduce the fraction of HF exact exchange to 50% as in r^{2}SCAN@r^{2}SCAN50 while producing a potentially lower density-driven error than r^{2}SCAN [71,164]. This method gives our dataset an MAE of $\sim$0.75 eV/O$_2$ [Fig. 2(c)] and an RMSE of $\sim$0.82 eV/O$_2$.

Here, we propose the r^{2}SCAN10@r^{2}SCAN, which iterates to self-consistency with the less expensive r^{2}SCAN, and requires only a single total-energy evaluation (not requiring a complete self-consistent field electronic relaxation) with the more costly global hybrid r^{2}SCAN10. Supposedly, r^{2}SCAN10@r^{2}SCAN corrects functional-driven errors by introducing 10% exact exchange in the functional while using r^{2}SCAN orbitals.

In Figs. 2(b) and 2(c), r^{2}SCAN10@r^{2}SCAN yields an MAE of $\sim$0.62 eV/O$_2$ and a RMSE of $\sim$0.71 eV/O$_2$, which are comparable in magnitude to the hybrid functional r^{2}SCAN10 but can be obtained at a far lower computational cost. Indeed, r^{2}SCAN10@r^{2}SCAN appears sufficient to correct the functional-driven error of r^{2}SCAN [Fig. 2(b)]. We propose a more general approach in the form of r^{2}SCAN10@r^{2}SCAN50 that corrects both functional-driven errors, including 10% exact exchange in total energy estimation, and density-driven errors with 50% exact exchange in the density (orbital) generation. Applying r^{2}SCAN10@r^{2}SCAN50 to our dataset results in an MAE of $\sim$0.43 eV/O$_2$ and an RMSE of $\sim$0.57 eV/O$_2$. r^{2}SCAN10@r^{2}SCAN50 is the most accurate approach in the r^{2}SCANY@r^{2}SCANX family.

The XC functional LAK is expected to predict more accurate band gaps, which are closely related to charge-transfer processes in materials. For this reason, we expected that LAK might yield generally improved electron

TABLE II. Oxidation reactions and their experimental ΔH_0 (in eV/O$_2$) as defined in Eqs. (3) and (4).

Reaction	Change in oxidation state	ΔH_0
$2Ti_2O_3 + O_2 \rightarrow 4TiO_2$	$Ti^{3+} \rightarrow Ti^{4+}$	–7.6166 [128]
$4VO + O_2 \rightarrow 2V_2O_3$	$V^{2+} \rightarrow V^{3+}$	–7.3632 [127]
$\frac{4}{3}VO + O_2 \rightarrow \frac{2}{3}V_2O_5$	$V^{2+} \rightarrow V^{5+}$	–4.7469 [127]
$V_2O_3 + O_2 \rightarrow V_2O_5$	$V^{3+} \rightarrow V^{5+}$	–3.4387 [127]
$2VO + O_2 \rightarrow 2VO_2$	$V^{2+} \rightarrow V^{4+}$	–5.8368 [127]
$2V_2O_3 + O_2 \rightarrow 4VO_2$	$V^{3+} \rightarrow V^{4+}$	–4.3104 [127]
$2VO_2 + O_2 \rightarrow V_2O_5$	$V^{4+} \rightarrow V^{5+}$	–2.5670 [127]
$2Cr_2O_3 + O_2 \rightarrow 4CrO_2$	$Cr^{3+} \rightarrow Cr^{4+}$	–0.7286 [127]
$\frac{2}{3}Cr_2O_3 + O_2 \rightarrow \frac{4}{3}CrO_3$	$Cr^{3+} \rightarrow Cr^{6+}$	–0.2023 [127]
$2CrO_2 + O_2 \rightarrow 2CrO_3$	$Cr^{4+} \rightarrow Cr^{6+}$	0.0608 [127]
$6MnO + O_2 \rightarrow 2Mn_3O_4$	$Mn^{2+} \rightarrow Mn^{2+}, Mn^{3+}$	–4.7862 [127]
$2MnO + O_2 \rightarrow 2MnO_2$	$Mn^{2+} \rightarrow Mn^{4+}$	–2.7942 [127]
$Mn_3O_4 + O_2 \rightarrow 3MnO_2$	$Mn^{2+}, Mn^{3+} \rightarrow Mn^{4+}$	–1.7982 [127]
$6FeO + O_2 \rightarrow 2Fe_3O_4$	$Fe^{2+} \rightarrow Fe^{2+}, Fe^{3+}$	–6.7038 [127]
$4FeO + O_2 \rightarrow 2Fe_2O_3$	$Fe^{2+} \rightarrow Fe^{3+}$	–6.0620 [127]
$4Fe_3O_4 + O_2 \rightarrow 6Fe_2O_3$	$Fe^{2+}, Fe^{3+} \rightarrow Fe^{3+}$	–4.7784 [127]
$6CoO + O_2 \rightarrow 2Co_3O_4$	$Co^{2+} \rightarrow Co^{2+}, Co^{3+}$	–3.9014 [128]
$2Cu_2O + O_2 \rightarrow 4CuO$	$Cu^{+} \rightarrow Cu^{2+}$	–2.8744 [128]
$2Ce_2O_3 + O_2 \rightarrow 4CeO_2$	$Ce^{3+} \rightarrow Ce^{4+}$	–7.4238 [127]

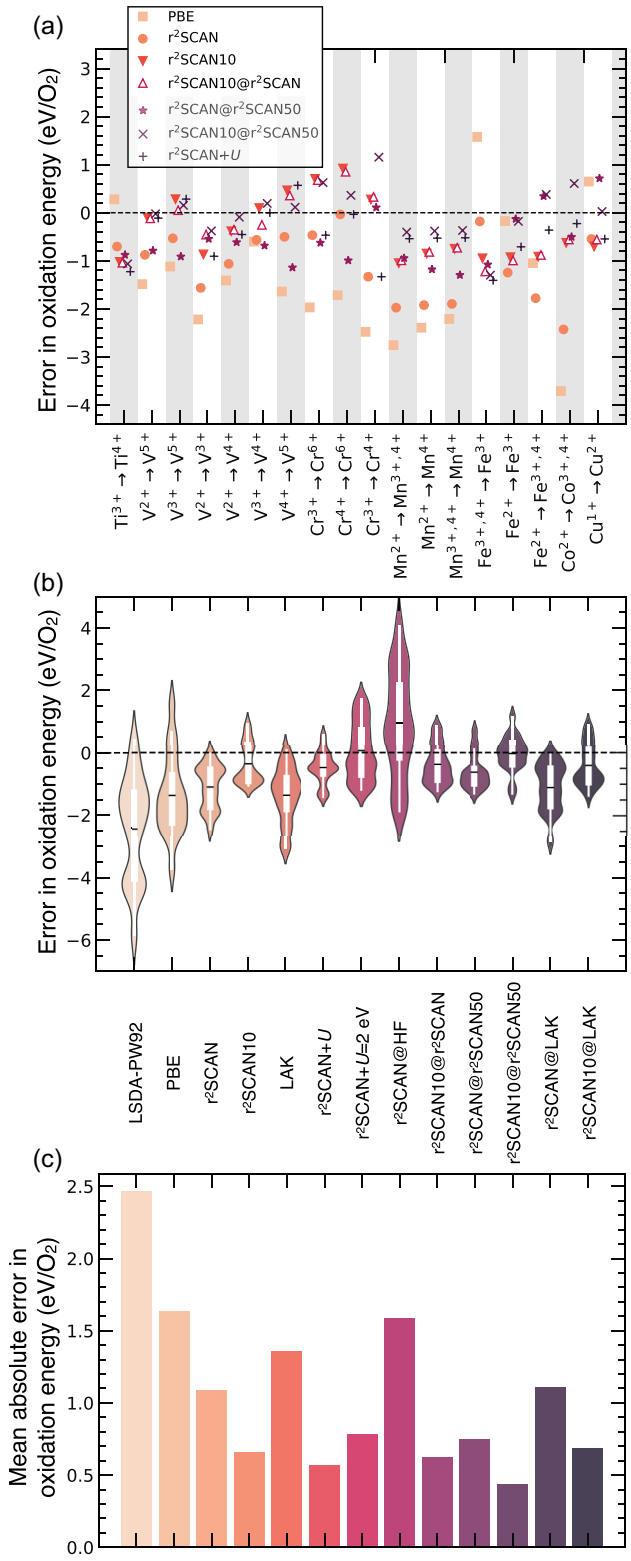

FIG. 2. Prediction error of $3d$ M_iO_j oxidation energies of reactions in Table II (except for Ce_iO_j compounds) with several XC functionals, including r^{2}SCANY@r^{2}SCANX and r^{2}SCANY@LAK as defined in Fig. 1. (a) Error in oxidation energies of 18 reactions considered. (b) Violin representation of error distributions. (c) The mean absolute errors. Errors in predicting oxidation energies of all DFT functionals except r^{2}SCAN + U are evaluated at r^{2}SCAN geometries. The mean experimental oxidation energy is –3.82 eV/O_2.

densities compared to r^{2}SCAN [23,165], and hence, speculatively, r^{2}SCAN@LAK and r^{2}SCAN10@LAK should predict oxidation energies in better agreement with experimental data. However, for our dataset, the performance of r^{2}SCAN@LAK (MAE: ∼1.12 eV/O_2) appears comparable to or slightly worse than that of r^{2}SCAN (MAE: ∼1.09 eV/O_2), and similarly, r^{2}SCAN10@LAK (MAE: ∼0.69 eV/O_2) shows no evident improvements over r^{2}SCAN10@r^{2}SCAN (MAE: ∼0.62 eV/O_2). Meanwhile, LAK gave a higher error compared to r^{2}SCAN, with a MAE of ∼1.36 eV/O_2 (RMSE ∼1.60 eV/O_2).

It is essential to analyze the type of distribution of oxidation energies in Fig. 2(b). In Fig. 2(b), oxidation energies with PBE form a largely unimodal distribution with a long tail towards positive error, comprising reactions such as Fe_3O_4 → Fe_2O_3, Cu_2O → CuO, Ti_2O_3 → TiO_2, and FeO → Fe_2O_3. The negative tail of this distribution is set by the reaction CoO → Co_3O_4. In contrast, r^{2}SCAN oxidation energies follow a bimodal distribution [Fig. 2(b)], with low- and high-error peaks. The low- (i.e., close to 0) error peak primarily comprises early transition metal, such as Ti, V, Cr, and Cu reactions. The high-error peak includes almost all the Mn, Fe, and Co reactions [Fig. 1(a)]. r^{2}SCAN10 and r^{2}SCAN10@r^{2}SCAN data also follow a bimodal distribution with low- and high-error peaks. Here, the low-error peak is centered on the zero-error line and consists of V and Cr reactions. The high-error peak is attributed to the reactions involving Ti, Mn, Fe, Co, and Cu species. Origins of bimodal distributions are discussed in detail in Sec. III B.

The distribution for r^{2}SCAN@r^{2}SCAN50 appears largely unimodal with a broad tail in the positive error comprising Cr_2O_3 → CrO_2 and Cu_2O → CuO reactions. r^{2}SCAN10@r^{2}SCAN50 also displays a unimodal distribution with the positive part encompassing the Cr_2O_3 → CrO_2 reaction, whereas the negative end of the tail gathers Ti_2O_3 → TiO_2 and Fe_3O_4 → Fe_2O_3.

To test the applicability of r^{2}SCANY@r^{2}SCANX on f-electron systems, we have applied it to the Ce_2O_3 → CeO_2 reaction (with prediction errors for this reaction in Supplemental Fig. 2 [126]). Experimentally, CeO_2 is NM (with no valence electron on Ce) [159], while Ce_2O_3 is AFM (with one f electron on Ce) [161]. Table I shows good agreement with the experiment for the r^{2}SCAN and r^{2}SCAN+U (U from Ref. [26]) lattice constants and magnetic moments.

At r^{2}SCAN, the Ce_2O_3 → CeO_2 reaction has an error of –0.95 eV/O_2. The error drops to 0.15 and 0.18 eV/O_2 for r^{2}SCAN10 and r^{2}SCAN10@r^{2}SCAN. However, using global hybrid densities in the DFA, the error surprisingly increases to ∼1.40 (r^{2}SCAN@r^{2}SCAN50) and ∼1.66 eV/O_2 (r^{2}SCAN10@r^{2}SCAN50), respectively. With r^{2}SCAN + U, the predicted oxidation energy is overestimated by ∼1.1 eV/O_2. For this reaction r^{2}SCAN@HF yields a large error of ∼5.76 eV/O_2, a very substantial underbinding of the extra O_2, aligning with observations of transition metal oxides.

D. Achieving optimal fractions of exact exchange in the r^{2}SCANY@r^{2}SCANX formulations

We now focus on potential improvements to the r^{2}SCAN functional, as elucidated in Fig. 1. We will explain how

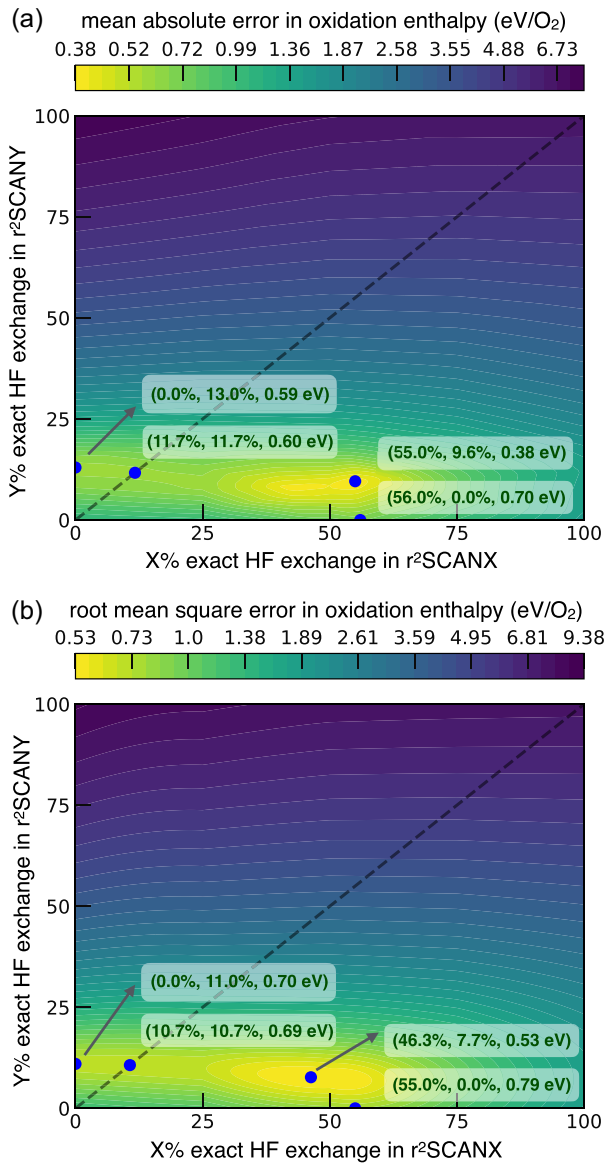

FIG. 3. Identification of optimal values of X and Y in r^2SCANY@r^2SCANX functionals, by locating minima in mean absolute and root mean square errors of oxidation energies of all possible oxidation reactions of M_iO_j's. (a) Shows that the mean absolute error minimizes at 55.0% exact exchange in orbitals and 9.6% exact exchange in the functional, forming r^2SCAN10@r^2SCAN55, which produces an error of ∼0.38 eV/O_2. (b) Shows that the root mean square error minimizes, with an error value of ∼0.53 eV at 46.3% exact exchange in orbital and 7.7% exact exchange in functional, thus r^2SCAN8@r^2SCAN46. See Sec. V for details on the interpolation scheme to coarse-grain values of X and Y.

optimal X and Y percentages of exact HF exchange are incorporated in the r^2SCAN functionals during the non-self-consistent and self-consistent steps. By utilizing all the oxidation energies predicted (Fig. 2) with various r^2SCANY@r^2SCANX functionals, we identify the optimal combination of X and Y percentages of HF exchange that minimizes their prediction errors in Fig. 3. In Supplemental Figs. 3–5 (which also show the individual reactions), the behavior of errors for individual reactions appears non-trivial; no correlation could be identified for any of the reactions [126]. Analysis of the MAE and RMSE trends in Figs. 3(a) and 3(b) for the self-consistent r^2SCANX and non-self-consistent r^2SCANY@r^2SCAN methods shows that the optimal exact-exchange fraction lies in the 9%–14% range.

Looking at the x axis of Figs. 3(a) and 3(b), for r^2SCAN@r^2SCANX, the minimum error (MAE and RMSE) is observed in the range ∼54%–58% exact HF exchange, indicating a significantly higher requirement for exact exchange in the Hamiltonian used for the orbital generation when the underlying functional is r^2SCAN. From the global minima in Figs. 3(a) and 3(b), the r^2SCANY@r^2SCANX approach achieves its lowest MAE and RMSE when Y—the HF fraction in the functional definition—is in the range of ∼7%–10%, and X (in the HF fraction in orbitals) is between ∼45% and 56%.

While the optimal exact exchange fraction varies across methods, a general trend shows errors are minimized with about ∼10% HF exchange in the functional and around ∼50% in orbital generation. These values balance the correction of density-functional-approximation SIEs.

E. Effects of exact-exchange fractions X and Y on the binding energy of the oxygen molecule

Figure 4 displays the error of O_2 binding energies introduced by several XC functionals, including the r^2SCANY@r^2SCANX proposed here. Figure 4(a) shows that all XC functionals considered here tend to overbind the O_2 molecule, with errors diminishing progressively from LSDA-PW92 (−2.2 eV/O_2) ≫ GGA PBE (−1.0 eV/O_2) ≫ meta-GGA r^2SCAN and LAK (−0.3 to − 0.2 eV/O_2) ≳ r^2SCANY@r^2SCANX.

Note that zero-point energy corrections are not included in this analysis and are a constant energy shift of ∼0.1 eV/O_2 [166,167]. The inadequacy of LSDA XC functionals, which overbinds the O_2 molecule, had already been noted by Perdew and Zunger [168] in agreement with LSDA-PW92 in Fig. 4(a). Similar inaccuracies were also identified for GGA functionals in Refs. [30,169].

Both LSDA and GGA strongly overestimate O_2 binding energy, causing systematic errors in predicted oxidation energies of M_iO_j's, which could be corrected *ad hoc* in Eq. (3). Both SCAN [20] and r^2SCAN [101] meta-GGA significantly alleviate the O_2 overbinding of PBE. In Fig. 4(a), the error in binding energy drops from ∼−1 eV/O_2 with PBE to ∼−0.3 eV/O_2 with r^2SCAN. However, a systematic error remains in r^2SCAN-predicted oxidation energies due to r^2SCAN overbinding O_2.

Figure 4 suggests that O_2 binding energies can be accurately predicted by r^2SCANY@r^2SCANX to eliminate systematic errors and achieve accurate oxidation energies of M_iO_j's. As indicated by the contour line in Fig. 4(b), setting Y at approximately 10% of the exact HF exchange in the non-self-consistent part, along with any value of X% for exact exchange in the orbital definition, results in a small error in O_2 binding energy (∼−0.03 eV/O_2).

In Fig. 4(a) r^2SCAN10, r^2SCAN10@r^2SCAN, and r^2SCAN10@r^2SCAN50 further reduce the error in O_2 binding energy to –0.031, –0.030, and 0.002 eV/O_2, respectively,

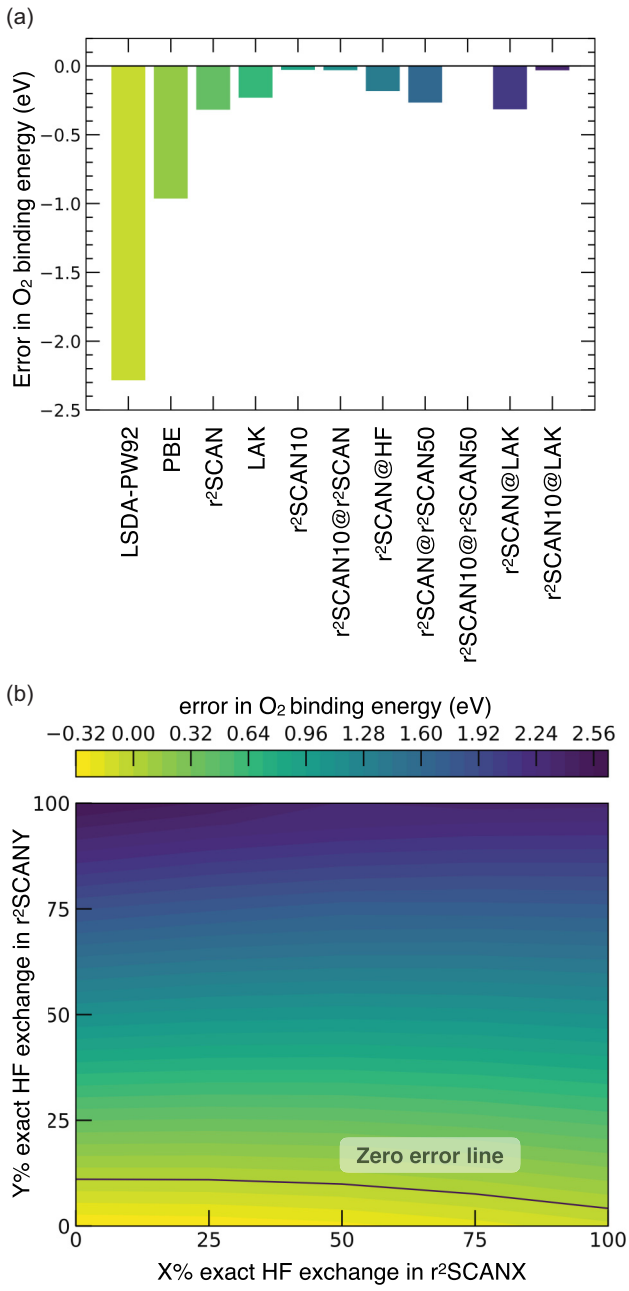

FIG. 4. Error in the negative binding energy of the O_2 molecule using r^{2}SCANY@r^{2}SCANX. (a) Shows the error for DFAs introduced in Fig. 1. All calculations are performed using r^{2}SCAN geometries. (b) Optimal values of X and Y, in various r^{2}SCANY@r^{2}SCANX functionals for O_2 binding energy, are demonstrated using the generalized r^{2}SCANY@r^{2}SCANX method. See Sec. V for details on the interpolation scheme to coarse-grain values of X and Y in (b).

thereby minimizing inaccuracies in predicting oxidation energies of M_iO_j's. Additionally, r^{2}SCAN@r^{2}SCAN50, which only deals with the density-driven error, does not seem to improve the O_2 binding energy error compared to r^{2}SCAN, indicating that the overbinding in O_2 binding energy is almost entirely due to the functional-driven error.

Using a harder projector augmented-wave (PAW) potential for oxygen (`O_h 06Feb2004` in VASP) overbinds the O_2 molecule, resulting in an increased error in O_2 binding energy of ∼0.15 eV/O_2 (see Supplemental Fig. 6) across all methods in Fig. 4 [126]. This increased error can be empirically mitigated by including the zero-point energy correction of ∼0.1 eV/O_2 [166,167].

F. Effects of exact-exchange fractions X and Y on on-site magnetic moments

The strong correlation in M_iO_j's seems to be captured at least in part by the DFA for normal correlation through spin symmetry breaking [25,170–173]. Here, we have used experimental or nearly experimental magnetic orders (Table I).

The artificial delocalization of d electrons due to SIE of XC functionals affects the predicted on-site magnetic moments in transition metals [47,48,52,68,174–176]. We investigate the variation in the error of predicted magnetic moments in our r^{2}SCANY@r^{2}SCANX. The magnetic moments are calculated by integrating the net spin density over the projector augmented-wave (PAW) potential spheres of the transition metal atoms.

The calculated on-site magnetic moments of transition metals depend only on the accuracy of electronic orbitals, particularly the fraction of exact exchange used in generating those orbitals. The on-site magnetic moments can be considered independent of the functional or the percentage of exact HF exchange employed in the non-self-consistent step (i.e., Y in r^{2}SCANY@r^{2}SCANX), which only affects the total energy evaluation and not the electronic charge density. Therefore, only the X percent of the exact exchange in r^{2}SCANY@r^{2}SCANX is relevant.

Figures 5(a) and 5(b) show the mean percent and absolute errors in magnetic moments of M_iO_j's. Increasing the percentage X of Hartree-Fock exchange increases the on-site magnetic moment associated with d electrons. For example, in Fe_2O_3, the average magnetic moment on Fe atoms increases from $3.86\mu_B$ with r^{2}SCAN to $4.01\mu_B$ with r^{2}SCAN10, $4.31\mu_B$ with r^{2}SCAN50, $4.48\mu_B$ with r^{2}SCAN100, and $4.51\mu_B$ with Hartree-Fock, i.e., X = 100% and no correlation in the DFA. This trend aligns with the expected behavior of hybrid functionals, enhancing the localization of magnetic moments. Supplemental Table 3 delineates this trend for all M_iO_j's [126].

From Fig. 5(a), the percent MAE and RMSE of magnetic moments are minimized in an interval of HF exact exchange in the r^{2}SCANX functional definition. There is no significant improvement in percent MAE for HF fractions larger than 30%, whereas percent RMSE increases progressively. Conversely, as shown in Fig. 5(b), the absolute magnitude of errors in magnetic moments decreases gradually as the fraction of exact HF exchange increases in defining the orbitals.

Figures 5(c) and 5(d) demonstrate that, starting from r^{2}SCAN magnetic moments, r^{2}SCAN50 reduces the MAE by 29%, and HF reduces it by 34%. In contrast, r^{2}SCAN + U (r^{2}SCAN + U = 2 eV) reduces error only by about 17% (15%). The MAE is especially sensitive to M_iO_j's with larger magnetic moments (e.g., MnO, FeO, Fe_2O_3, and Fe_3O_4 in Table I), where relatively small fractional moment changes

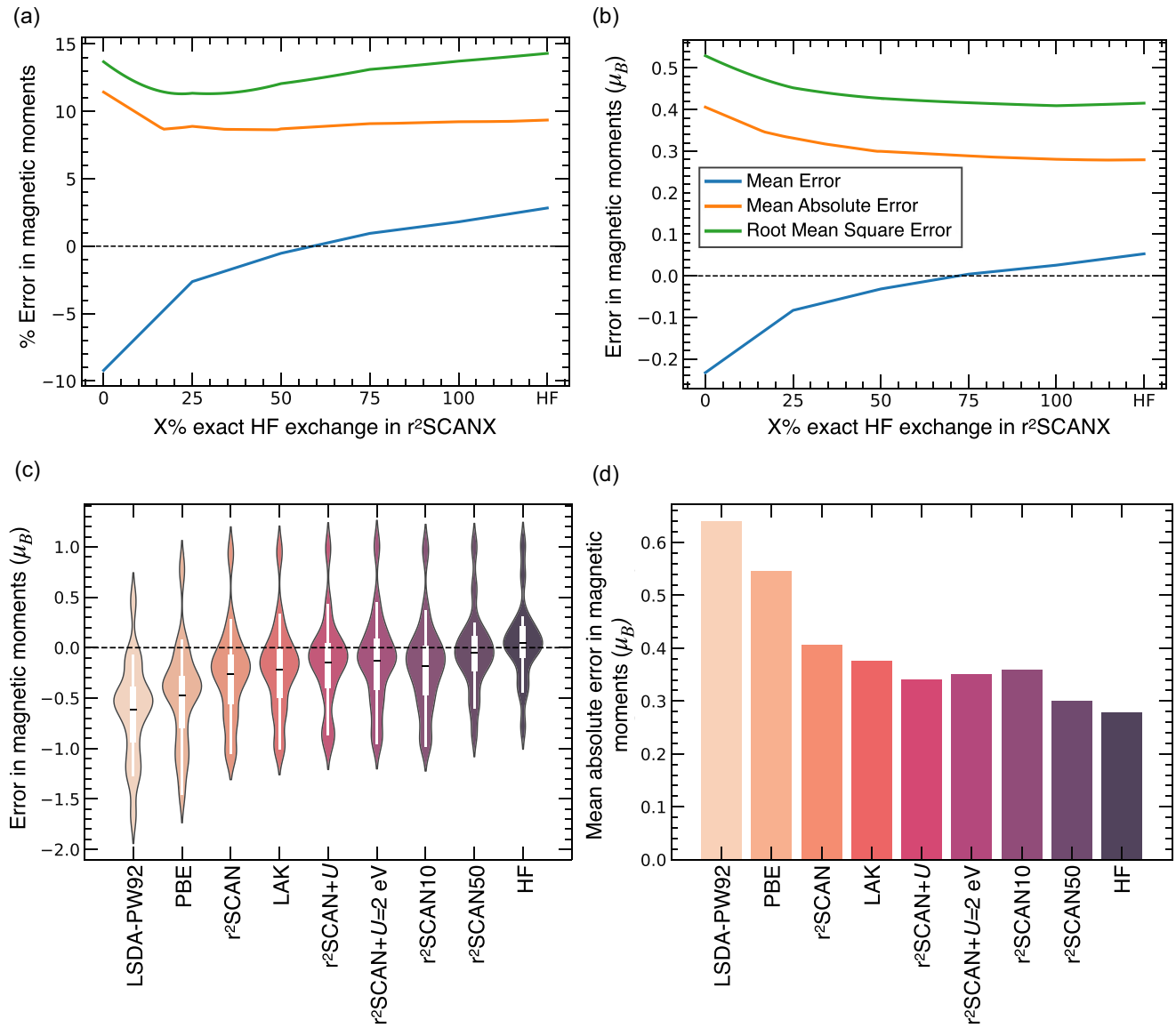

FIG. 5. Prediction errors of magnetic moments of M_iO_j's. (a) and (b) Show percent and nonrelative errors in magnetic moments vs X% exact HF exchange in r^{2}SCANX. (c) and (d) Show distributions and mean absolute errors of magnetic moments for selected DFAs introduced in Fig. 1. The mean experimental magnetic moment is $\sim 3.03 \mu_B$. See Supplemental Table 3 for numerical values of computed magnetic moments [126].

lead to larger absolute differences. However, the fact that the distribution center in Fig. 5(c) falls near the zero-error line indicates that r^{2}SCAN50 yields a better electron density in this sense. Figures 5(c) and 5(d) show an improvement from LAK over r^{2}SCAN by only about 7% for the magnetic moments.

G. Effects of exact-exchange fractions X and Y on the prediction of fundamental band gaps

Band gaps of materials are typically affected by SIE, with band gaps often underestimated by LSDA, GGA, and meta-GGA functionals [26,27,39,40,100,177–179]. We investigate the error in predicted band gaps using our r^{2}SCANY@r^{2}SCANX method. The fundamental band gap is the difference between the lowest unoccupied and the highest occupied orbital energies. Our orbital energies are expectation values of the r^{2}SCANY one-electron generalized Kohn-Sham Hamiltonian using the r^{2}SCANX orbitals. Y = 100% includes the full Fock operator and strongly overestimates band gaps.

Figures 6(a) and 6(b) show the MAE and the RMSE in predicted band gaps using the r^{2}SCANY@r^{2}SCANX method. Predicted band gaps with r^{2}SCANY@r^{2}SCANX depend on both the X% of exact HF exchange in the functional for the orbitals and the Y% of exact HF exchange in the functional used in the non-self-consistent step to evaluate the orbital energies. For M_iO_j's (Table I), Figures 6(a) and 6(b) show that the MAE minimizes at ∼7.3% exact HF exchange is used in the orbital generation (i.e., r^{2}SCANX), and around ∼8.6% exact HF exchange in the functional used in the non-self-consistent step (r^{2}SCANY). Similarly, the RMSE is

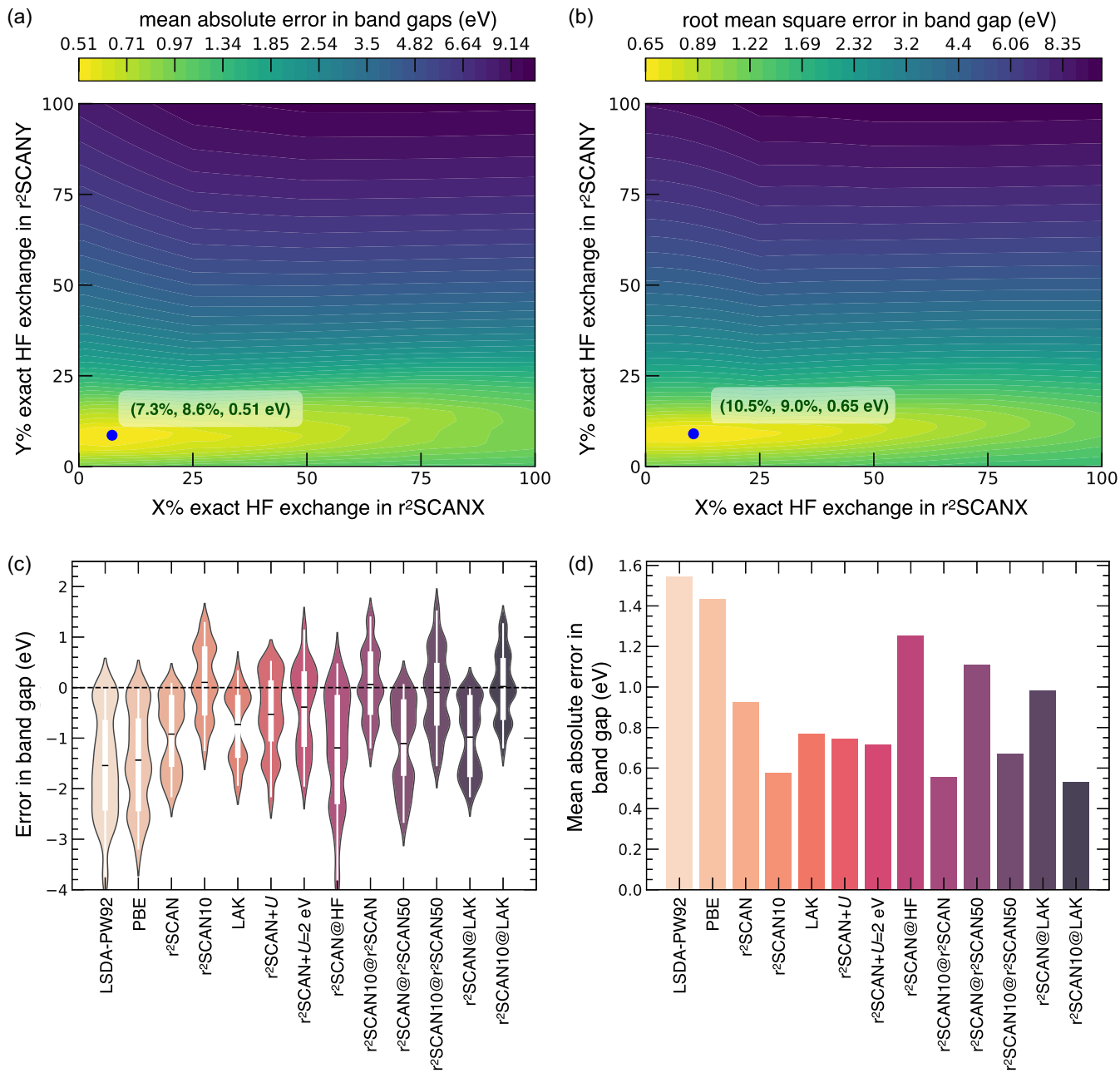

FIG. 6. Error in the fundamental band gap of M_iO_j's. (a) and (b) Display the mean absolute and root mean square errors in band gaps for the generalized r^{2}SCANY@r^{2}SCANX functionals. Likewise, (c) and (d) show the distribution and mean absolute errors in band gap for various r^{2}SCANY@r^{2}SCANX. See Sec. V for details on the interpolation scheme adopted to coarse-grain the values of X and Y of (a) and (b). The mean band gap of M_iO_j is ∼2.11 eV. See Supplemental Tables 4 and 5 for numerical values of computed band gaps [126].

minimized at ∼10.5% exact HF exchange, used in the orbital generation (i.e., r^{2}SCANX), and around ∼9.0% exact HF exchange in the functional used in the non-self-consistent step (r^{2}SCANY). Indeed, the predicted band gaps attain an optimal value for Y (∼9%), and the error increases rapidly beyond this. In contrast, the error increases slowly as X increases, reaching an optimal value.

Figure 6(c) is the error distribution, and Fig. 6(d) is the mean absolute error in predicted band gaps with XC functionals of Fig. 1. In Fig. 6(b) the MAE in band gaps systematically decreases from 1.54 eV for LSDA (PW91) > 1.43 eV for GGA(PBE) ≫ 0.93 eV in r^{2}SCAN, and > 0.77 eV for LAK, following the number of exact constraints satisfied by the DFAs in that sequence.

Turning our attention to r^{2}SCANY@r^{2}SCANX-type functionals, r^{2}SCAN10, r^{2}SCAN10@r^{2}SCAN, and r^{2}SCAN10@LAK have similar MAE errors of ∼0.53–0.58 eV, with a noticeable improvement over r^{2}SCAN. However, r^{2}SCAN@r^{2}SCAN50, which performed well for oxidation energies, performs poorly in predicting band gaps, with a substantial MAE of ∼1.11 eV. This error increase mainly comes from three closed d-shell oxides: TiO_2, V_2O_5, and CrO_3 (Supplemental Fig. 7) [126]. Notably, r^{2}SCAN + U (r^{2}SCAN + U = 2 eV) with a MAE error

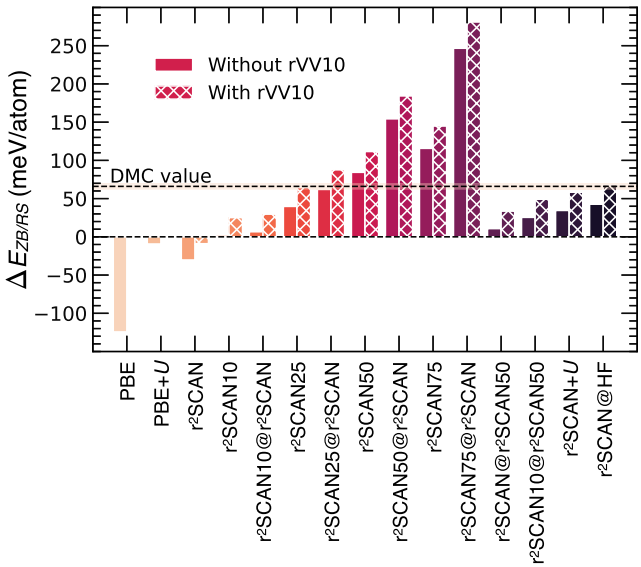

FIG. 7. Predicted relative energy difference between zinc blende (ZB) and rocksalt (RS) phases of MnO ($\Delta E_{ZB/RS}$) with a variety of r^{2}SCANY@r^{2}SCANX DFAs. Results for revised Vydrov-Van Voorhis 2010 (rVV10) van der Waals corrected r^{2}SCANY@r^{2}SCANX analogs are also shown. Values of $\Delta E_{ZB/RS}$ were computed using total energies from PAW potentials of *GW* type (as in Ref. [180]), where electrons from only 3*d* and 4*s* orbitals are explicitly considered. See Supplemental Fig. 8 for dependence of $\Delta E_{ZB/RS}$ on PAW potentials [126].

of ∼0.74 eV (∼0.71 eV) is outperformed by r^{2}SCAN10 (∼0.58 eV), r^{2}SCAN10@r^{2}SCAN (∼0.55 eV) and matched by r^{2}SCAN10@r^{2}SCAN50 (∼0.67 eV). NiO is often considered to be a prototype Mott insulator, [96,98] but its band gap (Supplemental Table 4) [126] is remarkably accurate with r^{2}SCAN10@r^{2}SCANX for X = 0 or 10.

H. Relative stability of MnO, NiO, and ZnO polymorphs with r^{2}SCANY@r^{2}SCANX approaches

A key quality of XC functionals is their ability to predict the correct polymorphism of transition-metal oxides accurately. A known issue with traditional DFAs concerns transition-metal monoxides MnO and CoO, which are predicted to be stable in the zinc blende (ZB) phase rather than the experimentally observed rocksalt (RS) structure [180–182]. This failure is common among GGA (PBE, see Fig. 7), GGA+*U* (or PBE+*U*), the range-separated hybrid HSE06, SCAN, and r^{2}SCAN DFA [180–182]. We will show that the r^{2}SCANY@r^{2}SCANX DFA reproduces the correct polymorphism of MnO.

In low-temperature experiments, MnO adopts a slightly distorted antiferromagnetic RS structure, while the ZB phase is not the bulk ground state. As shown in Fig. 7, PBE predicts the ZB structure as more stable than the RS polymorph, with a negative $\Delta E_{ZB/RS} \approx -244$ meV/f.u. [182]. Albeit with less negative values, r^{2}SCAN, and van der Waals corrected r^{2}SCAN+rVV10 cannot reproduce the correct MnO polymorphism. Adding a Hubbard *U* (PBE+*U*) or separately a pairwise vdW correction (TS-vdW) to the DFA reduces this error but still does not recover the RS ground state for MnO. Peng and Perdew showed that the correct polymorphism ($\Delta E_{ZB/RS} \approx 88$ meV/f.u.) is recovered by PBE+U + vdW [182]. Peng and Lany showed that the random phase approximation (RPA) can recover the RS phase as the ground state for MnO, with an energy difference $\Delta E_{ZB/RS} \approx +131$ meV/f.u. (+65.5 meV/atom) as shown in Fig. 7 [180]. This was confirmed by diffusion Monte Carlo (DMC) simulations, with $\Delta E_{ZB/RS} = 132 \pm 6.5$ meV/f.u. (66 meV/atom) [181]. Reference [182] demonstrated that SCAN+rVV10 + U produces a $\Delta E_{ZB/RS} \sim 135$ meV/f.u., reproducing the DMC and RPA data.

Figure 7 shows the predicted $\Delta E_{ZB/RS}$ with the r^{2}SCANY@r^{2}SCANX DFA. All r^{2}SCANY@r^{2}SCANX variants shown predict a positive $\Delta E_{ZB/RS}$ (in meV/atom), correctly stabilizing RS MnO over the ZB polymorph, and in agreement with existing RPA/DMC benchmarks [180,181]. The inclusion of the nonlocal rVV10 correlation systematically increases $\Delta E_{ZB/RS}$, pushing the r^{2}SCANY@r^{2}SCANX and r^{2}SCAN + U predictions toward the DMC (RPA) value. Here, we have used a version of rVV10 adapted for r^{2}SCAN [183]. Figure 7 shows that r^{2}SCAN25@r^{2}SCAN, r^{2}SCAN10@r^{2}SCAN50, and r^{2}SCAN@HF (and their rVV10 van der Waals analogs) are in excellent quantitative agreement with DMC and RPA references.

Previous work has demonstrated that GGA+U, meta-GGA (SCAN), and range-separated hybrids (HSE06) all predict the correct polymorphs for FeO and NiO [182]. We further confirm these predictions for the antiferromagnetic NiO configuration with r^{2}SCAN and the selected r^{2}SCANY@r^{2}SCANX (see Supplemental Fig. 9) [126]. The relative stability of the nonmagnetic wurtzite ZnO phase to its RS and ZB polymorphs appears correctly described by r^{2}SCAN and r^{2}SCANY@r^{2}SCANX and in better quantitative agreement with RPA [180] than GGA results (Supplemental Fig. 10) [126].

III. DISCUSSION

Standard DFAs suffer from significant SIEs, especially when applied to strongly correlated open-shell transition-metal oxides (M_iO_j's). SIE leads to inaccuracies in predicting many essential properties of M_iO_j's, including their structural parameters, electronic and magnetic structures, and thermochemical data.

Hybrid XC functionals mix a fraction of exact HF exchange with DFA to improve the accuracy of the electronic structure, thereby correcting functional-driven errors, particularly the SIE. The amount of HF exchange remains a tunable parameter. A number of strategies have been proposed to tune the amount of HF exchange in the DFA [64,67,70–76,184]. We have shown that M_iO_j's oxidation energies generally improve when climbing the ladder from LSDA to PBE to r^{2}SCAN, but further improvement is needed.

Unsurprisingly, we have shown that admixing exact HF exchange with r^{2}SCAN achieves better electronic, magnetic, and oxidation energies of M_iO_j's. For example, r^{2}SCAN10 (with 10% HF exchange) reduced the error in oxidation energies by ∼40% and by ∼38% for band gaps of M_iO_j's compared to r^{2}SCAN. r^{2}SCAN10 also reduces overbinding in

O_2, which is important for the accurate prediction of oxidation energies of M_iO_j's.

A. Electron densities from Hartree-Fock, hybrids, and DFT+*U* approaches

HF also provides self-interaction-free, albeit uncorrelated, electronic charge densities. Electronic charge densities from HF or hybrid functionals can overcorrect or correct density-driven errors. We have demonstrated that HF (or hybrid functional) electronic charge densities can correct r^{2}SCAN (or its hybrids) total energies for M_iO_j's by proposing a generalized r^{2}SCANY@r^{2}SCANX method. We have found optimal combinations of HF exchange in the charge density and functional definitions, such as r^{2}SCAN10, r^{2}SCAN10@r^{2}SCAN, r^{2}SCAN@r^{2}SCAN50, and r^{2}SCAN10@r^{2}SCAN50, which reduce the mean absolute (and relative) errors of predicted electronic and magnetic properties, and oxidation energies of M_iO_j's.

We have demonstrated that r^{2}SCANY@r^{2}SCANX can match or outperform r^{2}SCAN + U. In predicting the oxidation energies of M_iO_j's, the r^{2}SCAN10@r^{2}SCAN50 performed best, with a mean absolute error of ∼0.43 eV/O_2, lower than the r^{2}SCAN + U 0.57 eV/O_2. This can be rationalized as independently correcting the functional-driven error with 10% exact HF exchange and the density-driven error with 50% HF exchange.

Kulik and collaborators demonstrated that the ability of DFT+U to localize electrons on transition metals can vary significantly from that of hybrid functionals; these latter tend to localize the minority spin density (of the transition metal) away from the metal, and towards oxygen atoms in transition metal complexes [185,186]. We observe the same behavior in M_iO_j's. In agreement with Kulik *et al*. [185,186], we also show that a higher fraction of HF exchange in the XC functional increases the on-site magnetic moments on transition metals in M_iO_j's, which is rationalized by the rise of majority spin in the d manifolds. Considering these observations, we can qualitatively state that an increasing amount of HF in the DFA increases the ionic character of M_iO_j's. We quantify these behaviors for Fe_2O_3 in Supplemental Fig. 11 by a change in minority- and majority-spin electron numbers [126]. In addition, Supplemental Fig. 12 shows a progressive increase in the electron number on the oxygen sites with increasing X in r^{2}SCANX [126]. This is preceded by a similar increase from LSDA to PBE to r^{2}SCAN. The electron number at the transition-atom site decreases with increasing values of X. Exceptions to this trend are the M_iO_j's where strong charge disproportionation of the transition metal is favored, for example, Fe_3O_4 (Fe^{3+} and Fe^{2+}), Mn_3O_4 (Mn^{3+} and Mn^{2+}).

In addition, in transition-metal complexes, Ref. [186] concluded that DFT+U charge densities might differ substantially from hybrid functionals. To test this observation, we compare r^{2}SCAN@r^{2}SCAN + U M_iO_j's band gaps and oxidation energies (Supplemental Fig. 13) to r^{2}SCAN and r^{2}SCAN10@r^{2}SCAN50 results [126]. We demonstrate that r^{2}SCAN@r^{2}SCAN + U oxidation energies and band gaps are comparable to r^{2}SCAN.

In contrast, when using HF densities with r^{2}SCAN, as in r^{2}SCAN@HF, we have shown that M_iO_j oxidation energies worsen compared to r^{2}SCAN. MAEs increased from 1.09 eV/O_2 at r^{2}SCAN to 1.59 eV/O_2 at r^{2}SCAN@HF. But, we demonstrated that the MAE in M_iO_j oxidation energies can be halved (with respect to r^{2}SCAN@HF) to ∼0.75 eV/O_2 when implementing hybrid electronic charge densities of r^{2}SCAN admixed with 50% HF exchange as in r^{2}SCAN@r^{2}SCAN50.

B. Sources of uncertainty and error

The widely accepted standard for representing uncertainties in experimentally obtained oxidation enthalpies and other thermochemical data requires estimates of the 95% confidence intervals, which all thermochemical tables universally follow [127,128,187]. Ruscic argued that the MAE of calculated formation energies relative to experimental ones underestimates the error of the calculated values [188]. For this reason, when benchmarking the accuracy of r^{2}SCANY@r^{2}SCANX (Fig. 3), we also used the root mean square error.

Reproducing errorless O_2 binding energies is important for accurate predictions of oxidation energies of M_iO_j's. LSDA and PBE drastically overbind the O_2 molecule with large negative binding energies [30,168,169], ∼−2.2 eV/O_2 and ∼−1 eV/O_2, respectively, resulting in a systematic shift in predicted oxidation energies. With r^{2}SCAN, this negative error drops in magnitude to a sizable value of ∼−0.3 eV/O_2. Applying a constant shift (of –0.3 eV/O_2) to correct the spurious O_2 overbinding in r^{2}SCAN would further underestimate M_iO_j oxidation energies [see Fig. 2(a)], further exacerbating the error in r^{2}SCAN predictions. Previously, similar corrections have been applied to PBE O_2 and M_iO_j formation energies [30,31]. Notably, we have demonstrated that r^{2}SCAN10@r^{2}SCAN, r^{2}SCAN10, and r^{2}SCAN10@r^{2}SCAN50 decrease the error in the O_2 binding energy to values ⩽0.03 eV/O_2 in magnitude, and without requiring any fitting procedures [30,31].

Since the errors of O_2 binding energy are minimal with r^{2}SCANY@r^{2}SCANX methods, errors in the oxidation energies of M_iO_j's must reside in the prediction of the reduced and oxidized oxides. This is a bimodal distribution of r^{2}SCAN oxidation energies [Fig. 2(b)], consisting of a low (near-zero) peak for early transition-metal (Ti, V, Cr) reactions, and higher errors for late transition-metals (Mn, Fe, Co) reaction. Early transition metals (Ti, V, and Cr) with a small number of d electrons in their electronic configurations probably reduce correlation effects, which are more prominent for the late transition metals (Mn, Fe, and Co) with more d electrons. Furthermore, redox reactions involving transition metals' d-shell changes, such as $Ti^{4+}(d^0) \rightarrow Ti^{3+}(d^1)$, or $Cu^{+}(d^{10}) \rightarrow Cu^{2+}(d^9)$, appear to be in better agreement with experimental data. Milder correlation effects in closed-shell transition metals make r^{2}SCAN sufficient to describe the electronic structure of their oxides (TiO_2, V_2O_5, *etc*.).

From these observations, we expect that the electron density by r^{2}SCAN may be too delocalized to capture localization effects in late transition metals, i.e., Mn, Fe, Co, with a larger number of d electrons. Better electronic charge densities as provided by r^{2}SCAN@r^{2}SCAN50, correct the electron number in the d manifolds, recovering a unimodal

distribution [Fig. 2(b)], with a substantial decrease of oxidation energies errors for M_iO_j's with M = Mn, Fe, and Co. In addition, due to the functional-driven error, the average error of r^{2}SCAN@r^{2}SCAN50 is nonzero, resulting in an offset distribution around the zero-error line. In r^{2}SCAN10@r^{2}SCAN50 the functional-driven error reduces, and the unimodal distribution centers near the zero-error line.

Magnetic moments are also typically impacted by SIE and are underestimated due to the overdelocalization of $d(f)$ electrons on transition metals by GGA and meta-GGA functionals. As we climb the Jacob's ladder [189] of the XC functionals from LSDA (PW91) to GGA, and to meta-GGAs, the error in magnetic moments decreases accordingly, as shown by the functional MAE distributions of Figs. 5(a) and 5(b). We observed that the error in magnetic moments drops slowly as the percentage of HF exchange in the orbital increases. Compared to r^{2}SCAN, for r^{2}SCAN50, the error in magnetic moment reduces by ∼29%, and for HF, the error reduces by ∼34%. In contrast, r^{2}SCAN + U minimizes the error in magnetic moments only by ∼17%. Note that the variance in experimentally reported magnetic moments can be as high as $+1.00\mu_B$. For example, magnetic moments in V^{3+} in V_2O_3 are reported to vary between $1.2\mu_B$ and $2.37\mu_B$ (Table I) [131,132], which corresponds to variations larger than 100%. Note, we have neglected the orbital component of the magnetic moment and considered only the spin component. It has been shown that the orbital component can be substantial in specific cases. For example, 0.6–1μ_B for FeO [60,190–192], 1–1.6μ_B for CoO [60,190–199], 0.3–0.45μ_B for NiO [190,191,195,198,200], but can have negligible contributions in other oxides [201]. Despite this considerable uncertainty in experimentally reported magnetic moments and neglected orbital components, we observed a noticeable decrease in MAE of M_iO_j's predicted magnetic moments from r^{2}SCAN to r^{2}SCAN50.

Band gaps of M_iO_j's are typically underestimated by standard DFT predictions, with absolute errors rapidly decreasing as LSDA (PW92)>GGA (PBE)≫meta-GGAs (r^{2}SCAN and LAK)>hybrid meta-GGA (r^{2}SCANX) [see Figs. 6(c) and 6(d)]. Using r^{2}SCANY@r^{2}SCANX, we demonstrated that errors in band gaps are minimized with approximately 7%–11% exact exchange in the functional and the orbital definitions, which differs from the optimal HF fractions minimizing oxidation energy errors of M_iO_j's. We have shown that band gaps predicted by r^{2}SCAN10@r^{2}SCAN are more accurate than r^{2}SCAN + U, with MAEs of 0.55 eV/O_2 and 0.74 eV/O_2, respectively.

C. r^{2}SCANY@r^{2}SCANX as a generalization of single-shot and density-corrected approaches

The r^{2}SCANY@r^{2}SCANX approach resembles single-shot hybrid schemes, which serve as cost-effective proxies for fully self-consistent hybrid calculations in large-scale solid-state simulations with supercells containing hundreds or thousands of atoms. Single-shot hybrid approaches start with a self-consistent calculation using an inexpensive (semi)local DFA to get initial charge density and orbitals, then perform a one-shot non-self-consistent evaluation with a superior DFA, often a hybrid functional, based on those initial orbitals [202–214].

Single-shot approaches have been proven to produce band-gap-corrected single-particle and quasiparticle energies approaching the quality of hybrid DFAs or even *GW* quality for semiconductor alloys [202,203,205–210], transition-metal oxides [203,204], disordered phases [211], point defects [212], and interfaces [213,214].

Single-shot approaches can significantly improve prediction accuracy for errors in the DFA, such as inaccuracies in predicting orbital energies. Using a single non-self-consistent hybrid (or more advanced) evaluation based on a semilocal density functional can produce better orbital energies at much lower computational cost than a fully self-consistent hybrid calculation. This resembles the "single-shot" G_0W_0 variant of *GW*, employing a more accurate self-energy operator noniteratively on orbitals from inexpensive DFT calculations.

We generalized these approaches by replacing the single-shot hybrid type with parametrized global hybrid r^{2}SCANY and r^{2}SCANX for density, yielding r^{2}SCANY@r^{2}SCANX that addresses both functional- and density-driven inaccuracies.

It is worth noting that r^{2}SCANY@r^{2}SCANX is also a more general form of the density-corrected DFT, also known as DFA@HF, previously proposed in the literature [77–83].

D. False metals and structure symmetry breaking

Materials exhibit many degrees of freedom in their crystal structures. Deformation of cation polyhedra, polyhedra tilting, and Jahn-Teller distortions all decrease the crystal symmetry in materials [25,172]. Specific magnetic orderings of transition metals in M_iO_j's, accessible by neutron scattering and magnetic spectroscopies, further reduce crystal symmetries. On the one hand, standard structural techniques, such as X-ray and neutron diffraction, generally show less sensitivity to such distortions and defects. As such, the reported crystal structures may be inherently more symmetric than the actual structures. On the other hand, band-gap measurements are sensitive to symmetry-breaking motifs, defects in materials, and charge and magnetic orderings. Zunger and collaborators demonstrated that DFT of overly symmetrized M_iO_j's and other materials tends to close band gaps, predicting "false metals" [25,170–172,215].

Starting from the highly symmetrized experimental structures, further optimized with r^{2}SCAN, our r^{2}SCAN band-gap predictions of Ti_2O_3 [103], V_2O_3 [105], and Fe_3O_4 [116] is ∼0.0 eV (Table I). Upon removing all possible symmetry layers (perturbing atomic positions from high-symmetry sites of large supercell models, imposing ground-state magnetic orderings, removing intrinsic symmetry of wave functions, orbitals, and time reversal), Ti_2O_3, V_2O_3, and Fe_3O_4 remain metallic. However, the experimentally reported band gaps for Ti_2O_3, V_2O_3, and Fe_3O_4 are smaller than or equal to ∼0.2 eV (Table I), which makes band-gap opening unlikely, even with substantial symmetry breaking as demonstrated here. We found no structure symmetry breaking for Ti_2O_3 and V_2O_3, but observed it for Fe_3O_4.

There can be multiple symmetry breakings [25,170], and we may not have found the lowest-energy one. However,

Supplemental Table 4 shows that (without structure symmetry breaking) nonzero gaps in these materials arise in the self-consistent hybrid r^{2}SCAN10 [126].

E. Computational efficiency considerations of r^{2}SCANY@r^{2}SCANX approaches

We comment on the computational costs of r^{2}SCANY@r^{2}SCANX. With VASP, the self-consistent (SCF) global hybrids, such as r^{2}SCAN10, are ∼10–100 times more expensive than typical SCF r^{2}SCAN calculations. However, using the r^{2}SCAN10@r^{2}SCAN, which gives similar accuracy as SCF r^{2}SCAN10, the cost can be as low as ∼2–5 times that of SCF r^{2}SCAN, since it only requires one non-self-consistent evaluation of r^{2}SCAN10. Methods such as r^{2}SCAN@r^{2}SCAN50 and r^{2}SCAN10@r^{2}SCAN50 have a similar computational cost as global hybrids, as they require SCF r^{2}SCAN50 orbitals but provide improved accuracy over a SCF r^{2}SCAN10. The qualitative trend in the computational cost required for r^{2}SCANY@r^{2}SCANX is as follows: r^{2}SCAN $<$ r^{2}SCANY@r^{2}SCAN $\ll$ r^{2}SCANX $\approx$ r^{2}SCAN@r^{2}SCANX $\approx$ r^{2}SCANY@r^{2}SCANX.

IV. CONCLUSIONS

We have found that prediction accuracy for M_iO_j improves as more exact constraints and suitable non-bonded norms are met by approximating the density functional for exchange-correlation energy. We have developed r^{2}SCANY@r^{2}SCANX to mitigate the self-interaction error of exchange and correlation functionals for the accurate simulations of electronic, magnetic, and thermochemical properties of transition-metal oxides. r^{2}SCANY@r^{2}SCANX uses different fractions of exact exchange to define energy and density simultaneously: X affects the electronic density, and Y changes the density functional approximation of the total energy, addressing density- and functional-driven errors of the energy. While Y = 10 and X = 50 are fitted or optimized for the oxidation energies of the transition-metal oxides, they are also the values expected from experience with *s*-*p*-bonded systems, as at the end of Sec. I.

In r^{2}SCANY@r^{2}SCANX, we found a dependence of the X and Y optimal percentages of exact Hartree-Fock exchange justified by their performance on the M_iO_j oxidation energies, their magnetic moments, and band gaps. Predicted uncertainties are minimized for M_iO_j's oxidation energies by r^{2}SCAN10@r^{2}SCAN50, and band gaps with r^{2}SCAN10@r^{2}SCAN. These properties improve from LSDA to PBE to r^{2}SCAN to r^{2}SCAN10@r^{2}SCAN. Replacing a small part of r^{2}SCAN with the same amount of Hartree-Fock exchange is likely to have minimal impact on satisfying DFA constraints.

r^{2}SCANY@r^{2}SCANX improves predictions, outperforming the DFT(r^{2}SCAN)+U commonly used for strongly correlated materials. r^{2}SCAN10@r^{2}SCAN is computationally more affordable than hybrid functionals while maintaining comparable accuracy for oxidation energies and band gaps. Further studies should investigate the transferability of r^{2}SCANY@r^{2}SCANX to other correlated systems, such as ionically bound transition-metal fluorides or polyanion systems (e.g., phosphates and silicates) with strong covalent character.

Self-consistent r^{2}SCAN10, already reduces the MAE of the oxidation energies to ∼0.66 eV eV/O_2. r^{2}SCAN10 improves upon r^{2}SCAN, for transition-metal oxides and for *sp*-bonded systems [216]. r^{2}SCAN10 even gives oxide band gaps slightly better than r^{2}SCAN + U. For the prototype Mott insulator NiO, r^{2}SCAN10@r^{2}SCANX gives a remarkably accurate band gap for X = 0 or 10. To reduce the MAE of oxidation energies in M_iO_j's to ∼0.43 eV/O_2, r^{2}SCAN10@r^{2}SCAN50 is needed, which lowers the density-driven error of r^{2}SCAN and r^{2}SCAN10. The r^{2}SCAN10@r^{2}SCAN is nearly as accurate as the self-consistent r^{2}SCAN10 hybrid for oxidation energies.

This and recent works [83,85,86,93,95,216] suggest that, in many cases with main-group and transition-metal elements, the functional-driven errors of r^{2}SCAN energy differences can far exceed small density-driven errors. This allows significant improvements in r^{2}SCAN energy differences by performing the costly self-consistent iteration and geometry optimization with the efficient r^{2}SCAN (with van der Waals correction), then applying a more expensive nonlocal functional (e.g., a hybrid) in a single post-self-consistent calculation, as in r^{2}SCAN10@r^{2}SCAN.

Standard GGA global hybrids require approximately 25% of exact exchange. SCAN and r^{2}SCAN meta-GGAs have less self-interaction error than GGAs, with the most accurate self-consistent SCAN hybrid for main-group molecules using 10% exact exchange [217], aligning with r^{2}SCAN10 to reduce functional-driven errors in transition-metal oxides. The functional-driven error dominates the density-driven [87] error of the energy in main-group molecules [83,85,86]. The density-driven error is smaller and less sensitive to many density features, as expected from the variational principle for DFA energy, but more sensitive to long-range charge-transfer errors than other density errors [86]. 50% of exact exchange reduces the density-driven errors of the energy in transition-metal oxides, as in main-group molecules [83,85,86].

For structural energy differences in M_iO_j's, RPA is the accepted standard [180,218], capturing the correct long-range physics. RPA yields realistic van der Waals interactions and accurate long-range electron transfer in ionic materials, including transition-metal oxides, and corrects energy differences between polymorphs. RPA includes exact exchange and nearly exact long-range nonlocal correlation, but it is inaccurate at short distances. It is known that RPA provides very accurate electron densities for molecules [219,220], surpassing r^{2}SCAN and Hartree-Fock when compared to CCSD(T). The reason for that is unclear, but the RPA error for short-range correlation does not affect the density. RPA is similar to coupled-cluster double excitations, which keep the short-range or exchangelike correction to the correlation energy that RPA ignores. RPA, CCD, CCSD, and CCSD(T) are all accurate for the density, with accuracy likely improving in that order. The same correct long-range physics should be found in CCSD and CCSD(T). Our r^{2}SCAN10@r^{2}SCAN50+rVV10 appears to capture the same physics in a different way. While r^{2}SCAN50 strongly improves electron transfer relative to r^{2}SCAN, it is expected to be less accurate than r^{2}SCAN for

other features of the electron density to which the density-driven error of the energy is insensitive.

We believe that r^{2}SCAN10@r^{2}SCAN50 may accurately predict total energies and band gaps for many non-metallic solids with *s*, *p*, or *d* electrons, and may be similarly accurate for molecules. r^{2}SCAN is already reasonably accurate for many molecular and material geometries. It exhibits intermediate-range van der Waals interactions but requires a long-range correction, particularly for layered geometries. r^{2}SCAN10@r^{2}SCANX+rVV10 could be accurate for total and single-electron energies in many non-metallic or weakly metallic systems with *s*, *p*, and *d* valence electrons.

V. FIRST-PRINCIPLES CALCULATION DETAILS

All calculations presented here are performed using the DFT formalism, as implemented in the Vienna *Ab initio* Simulation Package (VASP) [221–223]. The PAW potentials describe the core electrons [224,225]. The electrons from 3*s*, 3*p*, 3*d*, and 4*s* orbitals are explicitly considered for the transition-metal atoms. Using a PAW set that treats fewer valence electrons explicitly (3*p*, 3*d*, and 4*s*) significantly impacts M_iO_j oxidation energies and band gaps (Supplemental Fig. 14) [126]. The kinetic energy cutoff for the plane waves was set to 700 eV, and the total energy was converged to 10^{-6} eV per cell. Various DFT exchange and correlation functionals were used in their collinear spin-polarized implementation. These are the LSDA-PW92 [18], the PBE [19], the r^{2}SCAN [101], and LAK [23]. Global hybrid r^{2}SCANX [78] calculations were performed with percentages X of Hartree-Fock exchange as discussed in the results. Ground-state magnetic orderings reported experimentally (Table I), often derived from neutron diffraction experiments, were imposed in all simulations of M_iO_j's.

Geometries (coordinates, volumes, and cell shapes) converged when the forces on all atoms were lower than 0.01 eV/Å. All properties were calculated with r^{2}SCAN geometries unless explicitly mentioned. All calculations in this work use a Γ-centered Monkhorst-Pack [226] grid. For structure relaxation, a *k* grid with a density of 48 *k* points per Å^{-1} is used for all systems. All other calculations used a *k* grid with a density of approximately 700 *k* points per reciprocal atom.

The global hybrid r^{2}SCANX orbitals were evaluated at the following percentages of exact Hartree-Fock exchange, with X = 0%, 10%, 25%, 50%, 75%, and 100%, respectively. The non-self-consistent field r^{2}SCANY energies were assessed with a fine grid of Y values, from 0% to 100%, with 5% intervals. In r^{2}SCANY@r^{2}SCANX calculations, we started from self-consistently converged r^{2}SCANX orbitals (`WAVECAR` in VASP), which are used for a non-self-consistent single electronic step (`ALGO = EIGENVAL`) with the r^{2}SCANY functional. A linear interpolation scheme was employed to obtain the energies, band gaps, and magnetic moments at intermediate fractions of exact HF exchange, not explicitly calculated.

Due to the high computational costs of global hybrids used in this work, all DFT calculations are performed using unit cells that can accommodate the expected experimental magnetic ordering for each transition-metal oxide. On-site magnetic moments of each transition-metal atom were obtained by integrating the spin density within the projection radius of the PAW potentials. Changes of such radii have a negligible influence on the numerical values of the magnetic moment.

For estimating band gaps with r^{2}SCANY@r^{2}SCANX, we utilize the orbitals obtained self-consistently with r^{2}SCANX, subsequently, and apply the r^{2}SCANY functional non-self-consistently on the same orbitals to obtain the one-electron eigenenergies. These one-electron eigenenergies are then used to calculate the band gap.

ACKNOWLEDGMENTS

The Welch Foundation is acknowledged for providing P.C. support from a Robert A. Welch Professorship at the Texas Center for Superconductivity (Grant No. L-E-001-19921203) and the Welch Foundation Grant No. E-2227-20250403. We are grateful for the support of the Research Computing Data Core at the University of Houston for assistance with the calculations carried out in this work. J.P.P. acknowledges support from the National Science Foundation under Grant No. DMR-2426275 and the Department of Energy, Office of Science, Basic Energy Sciences, under Grant No. DE-SC-0018331. A.R. acknowledges support from the Department of Energy. Office of Science, Basic Energy Sciences, under Grant No. DE-SC0026293. J.S. acknowledges support from the National Science Foundation under Grant No. DMR–2042618. We acknowledge Dr. Hong Tang for pointing out that Ti_2O_3 is dimerized and is a diamagnetic system. We thank the referees for suggesting calculations and clarifications.

P.C. and J.P.P. designed and supervised the project; H.R.G. prepared and performed the simulations, data collection, and data analysis; P.C., J.P.P., J.S., R.Z., Y.W., A.R., and A.P. contributed to the data analysis; H.R.G. and P.C. wrote the first draft of the manuscript; All authors contributed to the discussion and the final version of this manuscript.

The authors declare that they have no competing interests.

DATA AVAILABILITY

The data that support the findings of this article are openly available [227], embargo periods may apply.

[1] W. Kohn and L. J. Sham, Self-consistent equations including exchange and correlation effects, Phys. Rev. **140**, A1133 (1965).

[2] J. E. Saal, S. Kirklin, M. Aykol, B. Meredig, and C. Wolverton, Materials design and discovery with high-throughput density functional theory: The Open Quantum Materials Database (OQMD), JOM **65**, 1501 (2013).

[3] A. Jain, S. P. Ong, G. Hautier, W. Chen, W. D. Richards, S. Dacek, S. Cholia, D. Gunter, D. Skinner, G. Ceder, and K. A. Persson, Commentary: The materials project: A

materials genome approach to accelerating materials innovation, APL Mater. **1**, 011002 (2013).

[4] A. Zunger, Inverse design in search of materials with target functionalities, Nat. Rev. Chem. **2**, 0121 (2018).

[5] C. W. Park and C. Wolverton, Developing an improved crystal graph convolutional neural network framework for accelerated materials discovery, Phys. Rev. Mater. **4**, 063801 (2020).

[6] A. K. Cheetham, R. Seshadri, and F. Wudl, Chemical synthesis and materials discovery, Nat. Synth. **1**, 514 (2022).

[7] J. Schmidt, H.-C. Wang, T. F. T. Cerqueira, S. Botti, and M. A. L. Marques, A dataset of 175k stable and metastable materials calculated with the PBEsol and SCAN functionals, Sci. Data **9**, 64 (2022).

[8] S. Curtarolo, W. Setyawan, G. L. W. Hart, M. Jahnatek, R. V. Chepulskii, R. H. Taylor, S. Wang, J. Xue, K. Yang, O. Levy, M. J. Mehl, H. T. Stokes, D. O. Demchenko, and D. Morgan, AFLOW: An automatic framework for high-throughput materials discovery, Comput. Mater. Sci. **58**, 218 (2012).

[9] A. Merchant, S. Batzner, S. S. Schoenholz, M. Aykol, G. Cheon, and E. D. Cubuk, Scaling deep learning for materials discovery, Nature (London) **624**, 80 (2023).

[10] V. Stevanović, S. Lany, X. Zhang, and A. Zunger, Correcting density functional theory for accurate predictions of compound enthalpies of formation: Fitted elemental-phase reference energies, Phys. Rev. B **85**, 115104 (2012).

[11] C. Chen and S. P. Ong, A universal graph deep learning interatomic potential for the periodic table, Nat. Comput. Sci. **2**, 718 (2022).

[12] B. Deng, P. Zhong, K. Jun, J. Riebesell, K. Han, C. J. Bartel, and G. Ceder, CHGNet as a pretrained universal neural network potential for charge-informed atomistic modelling, Nat. Mach. Intell. **5**, 1031 (2023).

[13] I. Batatia, D. P. Kovács, G. Simm, C. Ortner, and G. Csányi, MACE: Higher order equivariant message passing neural networks for fast and accurate force fields, in *Advances in Neural Information Processing Systems*, edited by S. Koyejo, S. Mohamed, A. Agarwal, D. Belgrave, K. Cho, and A. Oh (Curran Associates, Inc., 2022), Vol. 35, pp. 11423–11436.

[14] B. Kanungo, J. Hatch, P. M. Zimmerman, and V. Gavini, Learning local and semi-local density functionals from exact exchange-correlation potentials and energies, Sci. Adv. **11**, eady8962 (2025).

[15] R. G. Parr and W. Yang, *Density-Functional Theory of Atoms and Molecules* (Oxford University Press, Oxford, UK, 1995).

[16] W. Koch and M. C. Holthausen, in *A Chemist's Guide to Density Functional Theory*, 1st ed., edited by M. C. Holthausen (Wiley-VCH, Weinheim, Germany, 2001).

[17] A. J. Cohen, P. Mori-Sánchez, and W. Yang, Insights into current limitations of density functional theory, Science **321**, 792 (2008).

[18] J. P. Perdew and Y. Wang, Accurate and simple analytic representation of the electron-gas correlation energy, Phys. Rev. B **45**, 13244 (1992).

[19] J. P. Perdew, K. Burke, and M. Ernzerhof, Generalized gradient approximation made simple, Phys. Rev. Lett. **77**, 3865 (1996).

[20] J. Sun, A. Ruzsinszky, and J. P. Perdew, Strongly constrained and appropriately normed semilocal density functional, Phys. Rev. Lett. **115**, 036402 (2015).

[21] J. W. Furness, Y. Zhang, C. Lane, I. G. Buda, B. Barbiellini, R. S. Markiewicz, A. Bansil, and J. Sun, An accurate first-principles treatment of doping-dependent electronic structure of high-temperature cuprate superconductors, Commun. Phys. **1**, 11 (2018).

[22] A. D. Kaplan, M. Levy, and J. P. Perdew, The predictive power of exact constraints and appropriate norms in density functional theory, Annu. Rev. Phys. Chem. **74**, 193 (2023).

[23] T. Lebeda, T. Aschebrock, and S. Kümmel, Balancing the contributions to the gradient expansion: Accurate binding and band gaps with a nonempirical meta-GGA, Phys. Rev. Lett. **133**, 136402 (2024).

[24] D. A. Kitchaev, H. Peng, Y. Liu, J. Sun, J. P. Perdew, and G. Ceder, Energetics of MnO_2 polymorphs in density functional theory, Phys. Rev. B **93**, 045132 (2016).

[25] Y. Zhang, J. Furness, R. Zhang, Z. Wang, A. Zunger, and J. Sun, Symmetry-breaking polymorphous descriptions for correlated materials without interelectronic U, Phys. Rev. B **102**, 045112 (2020).

[26] G. S. Gautam and E. A. Carter, Evaluating transition metal oxides within DFT-SCAN and SCAN+U frameworks for solar thermochemical applications, Phys. Rev. Mater. **2**, 095401 (2018).

[27] O. Y. Long, G. Sai Gautam, and E. A. Carter, Evaluating optimal U for 3d transition-metal oxides within the SCAN+U framework, Phys. Rev. Mater. **4**, 045401 (2020).

[28] N. Artrith, J. A. G. Torres, A. Urban, and M. S. Hybertsen, Data-driven approach to parameterize SCAN+U for an accurate description of 3d transition metal oxide thermochemistry, Phys. Rev. Mater. **6**, 035003 (2022).

[29] C. J. Bartel, A. W. Weimer, S. Lany, C. B. Musgrave, and A. M. Holder, The role of decomposition reactions in assessing first-principles predictions of solid stability, npj Comput. Mater. **5**, 4 (2019).

[30] L. Wang, T. Maxisch, and G. Ceder, Oxidation energies of transition metal oxides within the GGA +U framework, Phys. Rev. B **73**, 195107 (2006).

[31] A. Jain, G. Hautier, S. P. Ong, C. J. Moore, C. C. Fischer, K. A. Persson, and G. Ceder, Formation enthalpies by mixing GGA and GGA+U calculations, Phys. Rev. B **84**, 045115 (2011).

[32] R. S. Kingsbury, A. S. Rosen, A. S. Gupta, J. M. Munro, S. P. Ong, A. Jain, S. Dwaraknath, M. K. Horton, and K. A. Persson, A flexible and scalable scheme for mixing computed formation energies from different levels of theory, npj Comput. Mater. **8**, 195 (2022).

[33] J. Sun, R. C. Remsing, Y. Zhang, Z. Sun, A. Ruzsinszky, H. Peng, Z. Yang, A. Paul, U. Waghmare, X. Wu, M. L. Klein, and J. P. Perdew, Accurate first-principles structures and energies of diversely bonded systems from an efficient density functional, Nat. Chem. **8**, 831 (2016).

[34] Y. Zhang, J. Sun, J. P. Perdew, and X. Wu, Comparative first-principles studies of prototypical ferroelectric materials by LDA, GGA, and SCAN meta-GGA, Phys. Rev. B **96**, 035143 (2017).

[35] Y. Zhang, J. W. Furness, B. Xiao, and J. Sun, Subtlety of TiO_2 phase stability: Reliability of the density functional theory predictions and persistence of the self-interaction error, J. Chem. Phys. **150**, 014105 (2019).

[36] R. Zhang, B. Singh, C. Lane, J. Kidd, Y. Zhang, B. Barbiellini, R. S. Markiewicz, A. Bansil, and J. Sun, Critical role of mag-

netic moments in heavy-fermion materials: Revisiting SmB_6, Phys. Rev. B **105**, 195134 (2022).
[37] J. Ning, J. W. Furness, and J. Sun, Reliable lattice dynamics from an efficient density functional approximation, Chem. Mater. **34**, 2562 (2022).
[38] S. L. Dudarev, G. A. Botton, S. Y. Savrasov, C. J. Humphreys, and A. P. Sutton, Electron-energy-loss spectra and the structural stability of nickel oxide: An LSDA+U study, Phys. Rev. B **57**, 1505 (1998).
[39] D. B. Tekliye and G. Sai Gautam, Accuracy of metaGGA functionals in describing transition metal fluorides, Phys. Rev. Mater. **8**, 093801 (2024).
[40] S. Swathilakshmi, R. Devi, and G. S. Gautam, Performance of the r^{2}SCAN functional in transition metal oxides, J. Chem. Theory Comput. **19**, 4202 (2023).
[41] R. Devi, B. Singh, P. Canepa, and G. S. Gautam, Effect of exchange-correlation functionals on the estimation of migration barriers in battery materials, npj Comput. Mater. **8**, 160 (2022).
[42] N. E. Kirchner-Hall, W. Zhao, Y. Xiong, I. Timrov, and I. Dabo, Extensive benchmarking of DFT+U calculations for predicting band gaps, Appl. Sci. **11**, 2395 (2021).
[43] M. Cococcioni and S. De Gironcoli, Linear response approach to the calculation of the effective interaction parameters in the LDA + U method, Phys. Rev. B **71**, 035105 (2005).
[44] I. Timrov, N. Marzari, and M. Cococcioni, Hubbard parameters from density-functional perturbation theory, Phys. Rev. B **98**, 085127 (2018).
[45] M. Yu, S. Yang, C. Wu, and N. Marom, Machine learning the Hubbard U parameter in DFT+U using Bayesian optimization, npj Comput. Mater. **6**, 180 (2020).
[46] M. Uhrin, A. Zadoks, L. Binci, N. Marzari, and I. Timrov, Machine learning Hubbard parameters with equivariant neural networks, npj Comput. Mater. **11**, 19 (2025).
[47] F. Illas and R. L. Martin, Magnetic coupling in ionic solids studied by density functional theory, J. Chem. Phys. **108**, 2519 (1998).
[48] I. de P. R. Moreira, F. Illas, and R. L. Martin, Effect of Fock exchange on the electronic structure and magnetic coupling in NiO, Phys. Rev. B **65**, 155102 (2002).
[49] F. Corà, M. Alfredsson, G. Mallia, D. S. Middlemiss, W. C. Mackrodt, R. Dovesi, and R. Orlando, The performance of hybrid density functionals in solid state chemistry, in *Principles and Applications of Density Functional Theory in Inorganic Chemistry II*, Structure and Bonding Vol. 113 (Springer, Berlin, 2004), pp. 171–232.
[50] M. Alfredsson, G. D. Price, C. R. A. Catlow, S. C. Parker, R. Orlando, and J. P. Brodholt, Electronic structure of the antiferromagnetic $B1$-structured FeO, Phys. Rev. B **70**, 165111 (2004).
[51] M. Alfredsson, J. P. Brodholt, P. B. Wilson, G. D. Price, F. Corà, M. Calleja, R. Bruin, L. J. Blanshard, and R. P. Tyer, Structural and magnetic phase transitions in simple oxides using hybrid functionals, Mol. Simul. **31**, 367 (2005).
[52] F. Illas, I. de P. R. Moreira, J. M. Bofill, and M. Filatov, Spin symmetry requirements in density functional theory: The proper way to predict magnetic coupling constants in molecules and solids, Theor. Chem. Acc. **116**, 587 (2006).
[53] M. Marsman, J. Paier, A. Stroppa, and G. Kresse, Hybrid functionals applied to extended systems, J. Phys.: Condens. Matter **20**, 064201 (2008).
[54] J. L. F. Da Silva, M. V. Ganduglia-Pirovano, J. Sauer, V. Bayer, and G. Kresse, Hybrid functionals applied to rare-earth oxides: The example of ceria, Phys. Rev. B **75**, 045121 (2007).
[55] B. G. Janesko, T. M. Henderson, and G. E. Scuseria, Screened hybrid density functionals for solid-state chemistry and physics, Phys. Chem. Chem. Phys. **11**, 443 (2009).
[56] J. Paier, M. Marsman, and G. Kresse, Dielectric properties and excitons for extended systems from hybrid functionals, Phys. Rev. B **78**, 121201(R) (2008).
[57] V. L. Chevrier, S. P. Ong, R. Armiento, M. K. Y. Chan, and G. Ceder, Hybrid density functional calculations of redox potentials and formation energies of transition metal compounds, Phys. Rev. B **82**, 075122 (2010).
[58] P. Canepa, E. Schofield, A. V. Chadwick, and M. Alfredsson, Comparison of a calculated and measured XANES spectrum of α-Fe_2O_3, Phys. Chem. Chem. Phys. **13**, 12826 (2011).
[59] J. Yang, S. Falletta, and A. Pasquarello, Range-separated hybrid functionals for accurate prediction of band gaps of extended systems, npj Comput. Mater. **9**, 108 (2023).
[60] F. Tran, P. Blaha, K. Schwarz, and P. Novák, Hybrid exchange-correlation energy functionals for strongly correlated electrons: Applications to transition-metal monoxides, Phys. Rev. B **74**, 155108 (2006).
[61] J. Graciani, A. M. Márquez, J. J. Plata, Y. Ortega, N. C. Hernández, A. Meyer, C. M. Zicovich-Wilson, and J. F. Sanz, Comparative study on the performance of hybrid DFT functionals in highly correlated oxides: The case of CeO_2 and Ce_2O_3, J. Chem. Theory Comput. **7**, 56 (2011).
[62] M. D. Radin and D. J. Siegel, Charge transport in lithium peroxide: relevance for rechargeable metal–air batteries, Energy Environ. Sci. **6**, 2370 (2013).
[63] D.-H. Seo, A. Urban, and G. Ceder, Calibrating transition-metal energy levels and oxygen bands in first-principles calculations: Accurate prediction of redox potentials and charge transfer in lithium transition-metal oxides, Phys. Rev. B **92**, 115118 (2015).
[64] J. H. Skone, M. Govoni, and G. Galli, Nonempirical range-separated hybrid functionals for solids and molecules, Phys. Rev. B **93**, 235106 (2016).
[65] T. Das, G. Di Liberto, S. Tosoni, and G. Pacchioni, Band gap of 3D metal oxides and quasi-2D materials from hybrid density functional theory: Are dielectric-dependent functionals superior? J. Chem. Theory Comput. **15**, 6294 (2019).
[66] A. D. Becke, Density-functional thermochemistry. III. The role of exact exchange, J. Chem. Phys. **98**, 5648 (1993).
[67] P. J. Stephens, F. J. Devlin, C. F. Chabalowski, and M. J. Frisch, *Ab initio* calculation of vibrational absorption and circular dichroism spectra using density functional force fields, J. Phys. Chem. **98**, 11623 (1994).
[68] C. Franchini, R. Podloucky, J. Paier, M. Marsman, and G. Kresse, Ground-state properties of multivalent manganese oxides: Density functional and hybrid density functional calculations, Phys. Rev. B **75**, 195128 (2007).
[69] A. Görling and M. Levy, Hybrid schemes combining the Hartree–Fock method and density-functional theory: Underlying formalism and properties of correlation functionals, J. Chem. Phys. **106**, 2675 (1997).

[70] J. P. Perdew, M. Ernzerhof, and K. Burke, Rationale for mixing exact exchange with density functional approximations, J. Chem. Phys. **105**, 9982 (1996).

[71] C. Adamo and V. Barone, Toward reliable density functional methods without adjustable parameters: The PBE0 model, J. Chem. Phys. **110**, 6158 (1999).

[72] J. Heyd, G. E. Scuseria, and M. Ernzerhof, Hybrid functionals based on a screened Coulomb potential, J. Chem. Phys. **118**, 8207 (2003).

[73] J. Jaramillo, G. E. Scuseria, and M. Ernzerhof, Local hybrid functionals, J. Chem. Phys. **118**, 1068 (2003).

[74] B. G. Janesko and G. E. Scuseria, Local hybrid functionals based on density matrix products, J. Chem. Phys. **127**, 164117 (2007).

[75] T. M. Henderson, B. G. Janesko, and G. E. Scuseria, Range separation and local hybridization in density functional theory, J. Phys. Chem. A **112**, 12530 (2008).

[76] B. G. Janesko, A. V. Krukau, and G. E. Scuseria, Self-consistent generalized Kohn-Sham local hybrid functionals of screened exchange: Combining local and range-separated hybridization, J. Chem. Phys. **129**, 124110 (2008).

[77] E. Clementi and S. J. Chakravorty, A comparative study of density functional models to estimate molecular atomization energies, J. Chem. Phys. **93**, 2591 (1990).

[78] P. M. W. Gill, B. G. Johnson, J. A. Pople, and M. J. Frisch, An investigation of the performance of a hybrid of Hartree-Fock and density functional theory, Int. J. Quantum Chem. **44**, 319 (1992).

[79] G. E. Scuseria, Comparison of coupled-cluster results with a hybrid of Hartree–Fock and density functional theory, J. Chem. Phys. **97**, 7528 (1992).

[80] N. Oliphant and R. J. Bartlett, A systematic comparison of molecular properties obtained using Hartree–Fock, a hybrid Hartree–Fock density-functional-theory, and coupled-cluster methods, J. Chem. Phys. **100**, 6550 (1994).

[81] B. G. Janesko and G. E. Scuseria, Hartree–Fock orbitals significantly improve the reaction barrier heights predicted by semilocal density functionals, J. Chem. Phys. **128**, 244112 (2008).

[82] P. Verma, A. Perera, and R. J. Bartlett, Increasing the applicability of DFT I: Non-variational correlation corrections from Hartree–Fock DFT for predicting transition states, Chem. Phys. Lett. **524**, 10 (2012).

[83] B. Kanungo, A. D. Kaplan, C. Shahi, V. Gavini, and J. P. Perdew, Unconventional error cancellation explains the success of Hartree–Fock density functional theory for barrier heights, J. Phys. Chem. Lett. **15**, 323 (2024).

[84] G. Santra and J. M. Martin, What types of chemical problems benefit from density-corrected DFT? A probe using an extensive and chemically diverse test suite, J. Chem. Theory Comput. **17**, 1368 (2021).

[85] A. D. Kaplan, C. Shahi, R. K. Sah, P. Bhetwal, B. Kanungo, V. Gavini, and J. P. Perdew, How does HF-DFT achieve chemical accuracy for water clusters? J. Chem. Theory Comput. **20**, 5517 (2024).

[86] N. Pangeni, C. Shahi, J. P. Perdew, V. Subramanian, B. Kanungo, V. Gavini, and A. Ruzsinszky, Hartree-fock density functional theory works through error cancellation for the interaction energies of halogen and chalcogen bonded complexes, J. Chem. Phys. **164**, 064309 (2026).

[87] M.-C. Kim, E. Sim, and K. Burke, Understanding and reducing errors in density functional calculations, Phys. Rev. Lett. **111**, 073003 (2013).

[88] A. Wasserman, J. Nafziger, K. Jiang, M.-C. Kim, E. Sim, and K. Burke, The importance of being inconsistent, Annu. Rev. Phys. Chem. **68**, 555 (2017).

[89] E. Sim, S. Song, and K. Burke, Quantifying density errors in DFT, J. Phys. Chem. Lett. **9**, 6385 (2018).

[90] S. Vuckovic, S. Song, J. Kozlowski, E. Sim, and K. Burke, Density functional analysis: The theory of density-corrected DFT, J. Chem. Theory Comput. **15**, 6636 (2019).

[91] J. P. Perdew, R. G. Parr, M. Levy, and J. L. Balduz, Density-functional theory for fractional particle number: Derivative discontinuities of the energy, Phys. Rev. Lett. **49**, 1691 (1982).

[92] P. Mori-Sánchez, A. J. Cohen, and W. Yang, Many-electron self-interaction error in approximate density functionals, J. Chem. Phys. **125**, 201102 (2006).

[93] A. D. Kaplan, C. Shahi, P. Bhetwal, R. K. Sah, and J. P. Perdew, Understanding density-driven errors for reaction barrier heights, J. Chem. Theory Comput. **19**, 532 (2023).

[94] P. D. Mezei, G. I. Csonka, and M. Kállay, Electron density errors and density-driven exchange-correlation energy errors in approximate density functional calculations, J. Chem. Theory Comput. **13**, 4753 (2017).

[95] M. Gubler, M. R. Schäfer, J. Behler, and S. Goedecker, Accuracy of charge densities in electronic structure calculations, J. Chem. Phys. **162**, 094103 (2025).

[96] G. A. Sawatzky and J. W. Allen, Magnitude and origin of the band gap in NiO, Phys. Rev. Lett. **53**, 2339 (1984).

[97] J. Zaanen, G. A. Sawatzky, and J. W. Allen, Band gaps and electronic structure of transition-metal compounds, Phys. Rev. Lett. **55**, 418 (1985).

[98] V. I. Anisimov, J. Zaanen, and O. K. Andersen, Band theory and Mott insulators: Hubbard *U* instead of Stoner *I*, Phys. Rev. B **44**, 943 (1991).

[99] M. Imada, A. Fujimori, and Y. Tokura, Metal-insulator transitions, Rev. Mod. Phys. **70**, 1039 (1998).

[100] S. Lany, Semiconducting transition metal oxides, J. Phys.: Condens. Matter **27**, 283203 (2015).

[101] J. W. Furness, A. D. Kaplan, J. Ning, J. P. Perdew, and J. Sun, Accurate and numerically efficient r^{2}SCAN meta-generalized gradient approximation, J. Phys. Chem. Lett. **11**, 8208 (2020).

[102] K. Sugiyama and Y. Takéuchi, The crystal structure of rutile as a function of temperature up to 1600 °C, Z. Kristallogr. - Cryst. Mater. **194**, 305 (1991).

[103] S. C. Abrahams, Magnetic and crystal structure of titanium sesquioxide, Phys. Rev. **130**, 2230 (1963).

[104] S. Kumarakrishnan, N. L. Peterson, and T. O. Mason, Cation self-diffusion in disordered VO_x, J. Phys. Chem. Solids **46**, 1007 (1985).

[105] P. D. Dernier and M. Marezio, Crystal structure of the low-temperature antiferromagnetic phase of V_2O_3, Phys. Rev. B **2**, 3771 (1970).

[106] K. D. Rogers, An x-ray diffraction study of semiconductor and metallic vanadium dioxide, Powder Diffr. **8**, 240 (1993).

[107] R. Enjalbert and J. Galy, A refinement of the structure of V_2O_5, Acta Crystallogr. C **42**, 1467 (1986).

[108] A. H. Hill, A. Harrison, C. Dickinson, W. Zhou, and W. Kockelmann, Crystallographic and magnetic studies of mesoporous eskolaite, Cr_2O_3, Microporous Mesoporous Mater. **130**, 280 (2010).

[109] J. S. Stephens and D. W. J. Cruickshank, The crystal structure of $(CrO_3)_\infty$, Acta Crystallogr. B **26**, 222 (1970).

[110] P. Porta, M. Marezio, J. P. Remeika, and P. D. Dernier, Chromium dioxide: High pressure synthesis and bond lengths, Mater. Res. Bull. **7**, 157 (1972).

[111] S. Sasaki, K. Fujino, and Y. Takéuchi, X-ray determination of electron-density distributions in oxides, MgO, MnO, CoO, and NiO, and atomic scattering factors of their constituent atoms, Proc. Jpn. Acad. B **55**, 43 (1979).

[112] N. Curetti, D. Bernasconi, P. Benna, G. Fiore, and A. Pavese, High-temperature ramsdellite–pyrolusite transformation kinetics, Phys. Chem. Miner. **48**, 43 (2021).

[113] D. Jarosch, Crystal structure refinement and reflectance measurements of hausmannite, Mn_3O_4, Miner. Petrol. **37**, 15 (1987).

[114] C. Gökhan Ünlü, M. Burak Kaynar, T. Şimşek, A. Tekgül, B. Kalkan, and Ş. Özcan, Structure and magnetic properties of $(La_{1-x}Fe_x)FeO_3$ ($x = 0$, 0.25, 0.50) perovskite, J. Alloys Compd. **784**, 1198 (2019).

[115] A. Yamamoto, Modulated structure of wustite ($Fe_{1-x}O$) (three-dimensional modulation), Acta Crystallogr. B **38**, 1451 (1982).

[116] J. P. Wright, J. P. Attfield, and P. G. Radaelli, Charge ordered structure of magnetite Fe_3O_4 below the Verwey transition, Phys. Rev. B **66**, 214422 (2002).

[117] J. P. Picard, G. Baud, J. P. Besse, and R. Chevalier, Croissance cristalline et étude structurale de Co_3O_4, J. Less-Common Met. **75**, 99 (1980).

[118] Y. Deng, Z. Li, H. Wang, L. He, B. Zhang, and M. Zhang, Identification of the key structure factor to achieve high energy density in spinel $LiNi_{0.5}Mn_{1.5}O_4$, Chem. Mater. **36**, 8037 (2024).

[119] H. Yamada, Y. Soejima, X. G. Zheng, and M. Kawaminami, Structural study of CuO at low temperatures, Trans. Mater. Res. Soc. Jpn. **25**, 1199 (2000).

[120] R. Restori and D. Schwarzenbach, Charge density in cuprite, Cu_2O, Acta Crystallogr. B **42**, 201 (1986).

[121] S. C. Abrahams and J. L. Bernstein, Remeasurement of the structure of hexagonal ZnO, Acta Crystallogr. B **25**, 1233 (1969).

[122] D. Zagorac, H. Müller, S. Ruehl, J. Zagorac, and S. Rehme, Recent developments in the Inorganic Crystal Structure Database: Theoretical crystal structure data and related features, J. Appl. Crystallogr. **52**, 918 (2019).

[123] G. B. Jensen and O. V. Nielsen, The magnetic structure of Mn_3O_4 Hausmannite between 4.7 K and Neel point, 41 K, J. Phys. C: Solid State Phys. **7**, 409 (1974).

[124] R. M. Moon, T. Riste, W. C. Koehler, and S. C. Abrahams, Absence of antiferromagnetism in Ti_2O_3, J. Appl. Phys. **40**, 1445 (1969).

[125] Y. Zhang, D. Ke, J. Wu, C. Zhang, L. Hou, B. Lin, Z. Chen, J. P. Perdew, and J. Sun, Challenges for density functional theory in simulating metal–metal singlet bonding: A case study of dimerized VO_2, J. Chem. Phys. **160**, 134101 (2024).

[126] See Supplemental Material at http://link.aps.org/supplemental/10.1103/myd5-l4f4 for figures showing r^{2}SCANY@r^{2}SCANX errors in oxidation energies for all reactions studied, electron counts based on percent of exact HF exchange in different transition-metal oxides, relative polymorphic energies for NiO and ZnO phases, and tables of U values used in this work, alongside experimental formation energies from the literature. Supplemetal Material also includes tables of magnetic moments and band gaps calculated for the set of transition-metal oxides using various methods explored in this work.

[127] O. Kubaschewski and C. B. Alcock, in *Metallurgical Thermochemistry*, edited by G. V. Raynor, International Series on Materials Science and Technology Vol. 24, 5th ed. (Pergamon, Oxford, UK, 1979).

[128] T. C. Allison, NIST-JANAF Thermochemical Tables - SRD 13 (2013), https://janaf.nist.gov/.

[129] N. Serpone, Is the band gap of pristine TiO_2 narrowed by anion- and cation-doping of titanium dioxide in second-generation photocatalysts? J. Phys. Chem. B **110**, 24287 (2006).

[130] M. Uchida, J. Fujioka, Y. Onose, and Y. Tokura, Charge dynamics in thermally and doping induced insulator-metal transitions of $(Ti_{1-x}V_x)_2O_3$, Phys. Rev. Lett. **101**, 066406 (2008).

[131] R. M. Moon, Antiferromagnetism in V_2O_3, J. Appl. Phys. **41**, 883 (1970).

[132] S. Shin, Y. Tezuka, T. Kinoshita, A. Kakizaki, T. Ishii, Y. Ueda, W. Jang, H. Takei, Y. Chiba, and M. Ishigame, Observation of local magnetic moments in the Mott transition of V_2O_3 by means of 3s photoemission, Phys. Rev. B **46**, 9224 (1992).

[133] S. Shin, S. Suga, M. Taniguchi, M. Fujisawa, H. Kanzaki, A. Fujimori, H. Daimon, Y. Ueda, K. Kosuge, and S. Kachi, Vacuum-ultraviolet reflectance and photoemission study of the metal-insulator phase transitions inVO_2, V_6O_{13}, and V_2O_3, Phys. Rev. B **41**, 4993 (1990).

[134] J. B. Goodenough, The two components of the crystallographic transition in VO_2, J. Solid State Chem. **3**, 490 (1971).

[135] A. Kumar, P. Singh, N. Kulkarni, and D. Kaur, Structural and optical studies of nanocrystalline V_2O_5 thin films, Thin Solid Films **516**, 912 (2008).

[136] L. M. Corliss, J. M. Hastings, R. Nathans, and G. Shirane, Magnetic structure of Cr_2O_3, J. Appl. Phys. **36**, 1099 (1965).

[137] M. M. Abdullah, F. M. Rajab, and S. M. Al-Abbas, Structural and optical characterization of Cr_2O_3 nanostructures: Evaluation of its dielectric properties, AIP Adv. **4**, 027121 (2014).

[138] R. H. Misho, W. A. Murad, and G. H. Fattahallah, Preparation and optical properties of thin films of CrO_3 and Cr_2O_3 prepared by the method of chemical spray pyrolysis, Thin Solid Films **169**, 235 (1989).

[139] J. M. D. Coey and M. Venkatesan, Half-metallic ferromagnetism: Example of CrO_2, J. Appl. Phys. **91**, 8345 (2002).

[140] A. K. Cheetham and D. A. O. Hope, Magnetic ordering and exchange effects in the antiferromagnetic solid solutions $Mn_xNi_{1-x}O$, Phys. Rev. B **27**, 6964 (1983).

[141] L. Messick, W. C. Walker, and R. Glosser, Direct and temperature-modulated reflectance spectra of MnO, CoO, and NiO, Phys. Rev. B **6**, 3941 (1972).

[142] M. Regulski, R. Przeniosło, I. Sosnowska, and J.-U. Hoffmann, Incommensurate magnetic structure of β-MnO_2, Phys. Rev. B **68**, 172401 (2003).

[143] R. Druilhe and J. P. Suchet, Electron transport in CrO_2 and $Mn_xCr_{1-x}O_2$, Czech. J. Phys. **17**, 337 (1967).

[144] A. K. M. F. U. Islam, R. Islam, and K. A. Khan, Studies on the thermoelectric effect in semiconducting MnO_2 thin films, J. Mater. Sci.: Mater. Electron. **16**, 203 (2005).

[145] H. Y. Xu, S. L. Xu, X. D. Li, H. Wang, and H. Yan, Chemical bath deposition of hausmannite Mn_3O_4 thin films, Appl. Surf. Sci. **252**, 4091 (2006).

[146] W. L. Roth, Magnetic structures of MnO, FeO, CoO, and NiO, Phys. Rev. **110**, 1333 (1958).

[147] P. D. Battle and A. K. Cheetham, The magnetic structure of non-stoichiometric ferrous oxide, J. Phys. C: Solid State Phys. **12**, 337 (1979).

[148] H. Bowen, D. Adler, and B. Auker, Electrical and optical properties of FeO, J. Solid State Chem. **12**, 355 (1975).

[149] C. G. Shull, W. A. Strauser, and E. O. Wollan, Neutron diffraction by paramagnetic and antiferromagnetic substances, Phys. Rev. **83**, 333 (1951).

[150] T. Droubay, K. M. Rosso, S. M. Heald, D. E. McCready, C. M. Wang, and S. A. Chambers, Structure, magnetism, and conductivity in epitaxial Ti-doped α-Fe_2O_3 hematite: Experiment and density functional theory calculations, Phys. Rev. B **75**, 104412 (2007).

[151] S. K. Park, T. Ishikawa, and Y. Tokura, Charge-gap formation upon the Verwey transition in Fe_3O_4, Phys. Rev. B **58**, 3717 (1998).

[152] D. C. Khan and R. A. Erickson, Magnetic form factor of Co^{++} ion in cobaltous oxide, Phys. Rev. B **1**, 2243 (1970).

[153] P. Wei and Z. Q. Qi, Insulating gap in the transition-metal oxides: A calculation using the local-spin-density approximation with the on-site Coulomb U correlation correction, Phys. Rev. B **49**, 10864 (1994).

[154] J. van Elp, J. L. Wieland, H. Eskes, P. Kuiper, G. A. Sawatzky, F. M. F. de Groot, and T. S. Turner, Electronic structure of CoO, Li-doped CoO, and $LiCoO_2$, Phys. Rev. B **44**, 6090 (1991).

[155] W. Roth, The magnetic structure of Co_3O_4, J. Phys. Chem. Solids **25**, 1 (1964).

[156] B. X. Yang, J. M. Tranquada, and G. Shirane, Neutron scattering studies of the magnetic structure of cupric oxide, Phys. Rev. B **38**, 174 (1988).

[157] J. Ghijsen, L. H. Tjeng, J. van Elp, H. Eskes, J. Westerink, G. A. Sawatzky, and M. T. Czyzyk, Electronic structure of Cu_2O and CuO, Phys. Rev. B **38**, 11322 (1988).

[158] D. C. Reynolds, D. C. Look, B. Jogai, C. W. Litton, G. Cantwell, and W. C. Harsch, Valence-band ordering in ZnO, Phys. Rev. B **60**, 2340 (1999).

[159] T. Kolodiazhnyi, H. Sakurai, M. Avdeev, T. Charoonsuk, K. V. Lamonova, Y. G. Pashkevich, and B. J. Kennedy, Giant magnetocapacitance in cerium sesquioxide, Phys. Rev. B **98**, 054423 (2018).

[160] M. WoŁcyrz and L. Kepinski, Rietveld refinement of the structure of CeOCI formed in Pd/CeO_2 catalyst: Notes on the existence of a stabilized tetragonal phase of La_2O_3 in La-Pd-O system, J. Solid State Chem. **99**, 409 (1992).

[161] H. Pinto, M. Mintz, M. Melamud, and H. Shaked, Neutron diffraction study of Ce_2O_3, Phys. Lett. A **88**, 81 (1982).

[162] A. Prokofiev, A. Shelykh, and B. Melekh, Periodicity in the band gap variation of Ln_2X_3 (X = O, S, Se) in the lanthanide series, J. Alloys Compd. **242**, 41 (1996).

[163] H. Bärnighausen and G. Schiller, The crystal structure of A-Ce_2O_3, J. Less-Common Met. **110**, 385 (1985).

[164] M. Ernzerhof and G. E. Scuseria, Assessment of the Perdew–Burke–Ernzerhof exchange-correlation functional, J. Chem. Phys. **110**, 5029 (1999).

[165] T. Lebeda and S. Kümmel, Meta-GGA that describes weak interactions in addition to bond energies and band gaps, Phys. Rev. B **111**, 155133 (2025).

[166] J. A. Pople, M. Head-Gordon, D. J. Fox, K. Raghavachari, and L. A. Curtiss, Gaussian-1 theory: A general procedure for prediction of molecular energies, J. Chem. Phys. **90**, 5622 (1989).

[167] K. K. Irikura, Experimental vibrational zero-point energies: Diatomic molecules, J. Phys. Chem. Ref. Data **36**, 389 (2007).

[168] J. P. Perdew and A. Zunger, Self-interaction correction to density-functional approximations for many-electron systems, Phys. Rev. B **23**, 5048 (1981).

[169] P. E. Blöchl, First-principles calculations of defects in oxygen-deficient silica exposed to hydrogen, Phys. Rev. B **62**, 6158 (2000).

[170] G. Trimarchi, Z. Wang, and A. Zunger, Polymorphous band structure model of gapping in the antiferromagnetic and paramagnetic phases of the Mott insulators MnO, FeO, CoO, and NiO, Phys. Rev. B **97**, 035107 (2018).

[171] J. Varignon, M. Bibes, and A. Zunger, Origin of band gaps in 3d perovskite oxides, Nat. Commun. **10**, 1658 (2019).

[172] J.-X. Xiong, X. Zhang, and A. Zunger, Symmetry breaking forms split-off flat bands in quantum oxides controlling metal versus insulator phases, Phys. Rev. B **111**, 035154 (2025).

[173] J. P. Perdew, S. T. U. R. Chowdhury, C. Shahi, A. D. Kaplan, D. Song, and E. J. Bylaska, Symmetry breaking with the SCAN density functional describes strong correlation in the singlet carbon dimer, J. Phys. Chem. A **127**, 384 (2023).

[174] M. K. Horton, J. H. Montoya, M. Liu, and K. A. Persson, High-throughput prediction of the ground-state collinear magnetic order of inorganic materials using Density Functional Theory, npj Comput. Mater. **5**, 64 (2019).

[175] M. Arale Brännvall, G. Persson, L. Casillas-Trujillo, R. Armiento, and B. Alling, Predicting the Curie temperature of magnetic materials with automated calculations across chemistries and structures, Phys. Rev. Mater. **8**, 114417 (2024).

[176] G. Houchins and V. Viswanathan, Quantifying confidence in density functional theory predictions of magnetic ground states, Phys. Rev. B **96**, 134426 (2017).

[177] M. K. Y. Chan and G. Ceder, Efficient band gap prediction for solids, Phys. Rev. Lett. **105**, 196403 (2010).

[178] J. P. Perdew, W. Yang, K. Burke, Z. Yang, E. K. U. Gross, M. Scheffler, G. E. Scuseria, T. M. Henderson, I. Y. Zhang, A. Ruzsinszky, H. Peng, J. Sun, E. Trushin, and A. Görling, Understanding band gaps of solids in generalized Kohn–Sham theory, Proc. Natl. Acad. Sci. USA **114**, 2801 (2017).

[179] H. Peng and S. Lany, Semiconducting transition-metal oxides based on d^5 cations: Theory for MnO and Fe_2O_3, Phys. Rev. B **85**, 201202(R) (2012).

[180] H. Peng and S. Lany, Polymorphic energy ordering of MgO, ZnO, GaN, and MnO within the random phase approximation, Phys. Rev. B **87**, 174113 (2013).

[181] J. A. Schiller, L. K. Wagner, and E. Ertekin, Phase stability and properties of manganese oxide polymorphs: Assessment and

insights from diffusion Monte Carlo, Phys. Rev. B **92**, 235209 (2015).
[182] H. Peng and J. P. Perdew, Synergy of van der Waals and self-interaction corrections in transition metal monoxides, Phys. Rev. B **96**, 100101(R) (2017).
[183] J. Ning, M. Kothakonda, J. W. Furness, A. D. Kaplan, S. Ehlert, J. G. Brandenburg, J. P. Perdew, and J. Sun, Workhorse minimally empirical dispersion-corrected density functional with tests for weakly bound systems: r^2SCAN + rVV 10, Phys. Rev. B **106**, 075422 (2022).
[184] A. D. Becke, A new mixing of Hartree–Fock and local density-functional theories, J. Chem. Phys. **98**, 1372 (1993).
[185] T. Z. H. Gani and H. J. Kulik, Where does the density localize? Convergent behavior for global hybrids, range separation, and DFT+U, J. Chem. Theory Comput. **12**, 5931 (2016).
[186] Q. Zhao and H. J. Kulik, Where does the density localize in the solid state? Divergent behavior for hybrids and DFT+U, J. Chem. Theory Comput. **14**, 670 (2018).
[187] D. D. Wagman, W. H. Evans, V. B. Parker, R. H. Schumm, I. Halow, S. M. Bailey, K. L. Churney, and R. L. Nuttall, The NBS tables of chemical thermodynamic properties. Selected values for inorganic and C1 and C2 organic substances in SI units, J. Phys. Chem. Ref. Data **11**, Suppl. 2 (1982).
[188] B. Ruscic, Uncertainty quantification in thermochemistry, benchmarking electronic structure computations, and Active Thermochemical Tables, Int. J. Quantum Chem. **114**, 1097 (2014).
[189] J. P. Perdew and K. Schmidt, Jacob's ladder of density functional approximations for the exchange-correlation energy, AIP Conf. Proc. **577**, 1 (2001).
[190] A. Svane and O. Gunnarsson, Transition-metal oxides in the self-interaction–corrected density-functional formalism, Phys. Rev. Lett. **65**, 1148 (1990).
[191] R. Radwanski and Z. Ropka, First-principles consistent description of monoxides FeO, CoO and NiO, Phys. B: Condens. Matter **403**, 1453 (2008).
[192] A. Schrön and F. Bechstedt, Magnetic anisotropy of FeO and CoO: the influence of gradient corrections on exchange and correlation, J. Phys.: Condens. Matter **25**, 486002 (2013).
[193] I. V. Solovyev, A. I. Liechtenstein, and K. Terakura, Is Hund's second rule responsible for the orbital magnetism in solids? Phys. Rev. Lett. **80**, 5758 (1998).
[194] T. Shishidou and T. Jo, Antiferromagnetic structure in CoO, J. Phys. Soc. Jpn. **67**, 2637 (1998).
[195] W. Neubeck, C. Vettier, F. de Bergevin, F. Yakhou, D. Mannix, L. Ranno, and T. Chatterji, Orbital moment determination of simple transition metal oxides using magnetic x-ray diffraction, J. Phys. Chem. Solids **62**, 2173 (2001).
[196] W. Jauch and M. Reehuis, Electron density distribution in paramagnetic and antiferromagnetic CoO: A γ-ray diffraction study, Phys. Rev. B **65**, 125111 (2002).
[197] G. Ghiringhelli, L. H. Tjeng, A. Tanaka, O. Tjernberg, T. Mizokawa, J. L. de Boer, and N. B. Brookes, 3*d* spin-orbit photoemission spectrum of nonferromagnetic materials: The test cases of CoO and Cu, Phys. Rev. B **66**, 075101 (2002).
[198] R. Radwanski and Z. Ropka, Orbital moment in CoO and in NiO, Phys. B: Condens. Matter **345**, 107 (2004).
[199] A. Boussendel, N. Baadji, A. Haroun, H. Dreyssé, and M. Alouani, Effect of substrate strain on calculated magnetic properties and magnetic anisotropy energy of CoO, Phys. Rev. B **81**, 184432 (2010).
[200] V. Fernandez, C. Vettier, F. de Bergevin, C. Giles, and W. Neubeck, Observation of orbital moment in NiO, Phys. Rev. B **57**, 7870 (1998).
[201] F. Tran, G. Baudesson, J. Carrete, G. K. H. Madsen, P. Blaha, K. Schwarz, and D. J. Singh, Shortcomings of meta-GGA functionals when describing magnetism, Phys. Rev. B **102**, 024407 (2020).
[202] A. Alkauskas and A. Pasquarello, Effect of improved band-gap description in density functional theory on defect energy levels in α-quartz, Phys. B: Condens. Matter **401–402**, 670 (2007).
[203] F. Tran, On the accuracy of the non-self-consistent calculation of the electronic structure of solids with hybrid functionals, Phys. Lett. A **376**, 879 (2012).
[204] S. Lany, Band-structure calculations for the 3*d* transition metal oxides in *GW*, Phys. Rev. B **87**, 085112 (2013).
[205] S. Lany, A. N. Fioretti, P. P. Zawadzki, L. T. Schelhas, E. S. Toberer, A. Zakutayev, and A. C. Tamboli, Monte Carlo simulations of disorder in $ZnSnN_2$ and the effects on the electronic structure, Phys. Rev. Mater. **1**, 035401 (2017).
[206] T. Bischoff, J. Wiktor, W. Chen, and A. Pasquarello, Nonempirical hybrid functionals for band gaps of inorganic metal-halide perovskites, Phys. Rev. Mater. **3**, 123802 (2019).
[207] T. Bischoff, I. Reshetnyak, and A. Pasquarello, Adjustable potential probes for band-gap predictions of extended systems through nonempirical hybrid functionals, Phys. Rev. B **99**, 201114(R) (2019).
[208] S. R. Bauers, A. Holder, W. Sun, C. L. Melamed, R. Woods-Robinson, J. Mangum, J. Perkins, W. Tumas, B. Gorman, A. Tamboli, G. Ceder, S. Lany, and A. Zakutayev, Ternary nitride semiconductors in the rocksalt crystal structure, Proc. Natl. Acad. Sci. USA **116**, 14829 (2019).
[209] J. Yang, S. Falletta, and A. Pasquarello, One-shot approach for enforcing piecewise linearity on hybrid functionals: Application to band gap predictions, J. Phys. Chem. Lett. **13**, 3066 (2022).
[210] S. E. Gant, J. B. Haber, M. R. Filip, F. Sagredo, D. Wing, G. Ohad, L. Kronik, and J. B. Neaton, Optimally tuned starting point for single-shot *GW* calculations of solids, Phys. Rev. Mater. **6**, 053802 (2022).
[211] J. J. Cordell, G. J. Tucker, A. Tamboli, and S. Lany, Bandgap analysis and carrier localization in cation-disordered $ZnGeN_2$, APL Mater. **10**, 011112 (2022).
[212] P. Gorai, T. Famprikis, B. Singh, V. Stevanović, and P. Canepa, Devil is in the defects: Electronic conductivity in solid electrolytes, Chem. Mater. **33**, 7484 (2021).
[213] A. Sharan, M. Nardone, D. Krasikov, N. Singh, and S. Lany, Atomically thin interlayer phase from first principles enables defect-free incommensurate SnO_2/CdTe interface, Appl. Phys. Rev. **9**, 041411 (2022).
[214] Y. Xiong, C. Bourgois, N. Sheremetyeva, W. Chen, D. Dahliah, H. Song, J. Zheng, S. M. Griffin, A. Sipahigil, and G. Hautier, High-throughput identification of spin-photon interfaces in silicon, Sci. Adv. **9**, eadh8617 (2023).
[215] A. Zunger, J.-X. Xiong, and J. P. Perdew, Symmetry breaking transforms strong to normal correlation and false metals to true insulators, arXiv:2512.18236.
[216] R. Maniar, P. B. Shukla, J. K. Johnson, K. A. Jackson, and J. P. Perdew, Atomic ionization: sd energy imbalance and Perdew–

Zunger self-interaction correction energy penalty in 3d atoms, Proc. Natl. Acad. Sci. USA **122**, e2418305122 (2025).

[217] G. Santra and J. M. L. Martin, Pure and hybrid SCAN, rSCAN, and r^{2}SCAN: Which one is preferred in KS- and HF-DFT calculations, and how does D4 dispersion correction affect this ranking? Molecules **27**, 141 (2021).

[218] D. Pines, Emergent behavior in strongly correlated electron systems, Rep. Prog. Phys. **79**, 092501 (2016).

[219] E. Trushin, S. Fauser, A. Mölkner, J. Erhard, and A. Görling, Trushin *et al.* reply:, Phys. Rev. Lett. **135**, 019602 (2025).

[220] C. Shahi and J. P. Perdew, Comment on "accurate correlation potentials from the self-consistent random phase approximation", Phys. Rev. Lett. **135**, 019601 (2025).

[221] G. Kresse and J. Hafner, *Ab initio* molecular dynamics for liquid metals, Phys. Rev. B **47**, 558 (1993).

[222] G. Kresse and J. Furthmüller, Efficiency of *ab-initio* total energy calculations for metals and semiconductors using a plane-wave basis set, Comput. Mater. Sci. **6**, 15 (1996).

[223] G. Kresse and J. Furthmüller, Efficient iterative schemes for *ab initio* total-energy calculations using a plane-wave basis set, Phys. Rev. B **54**, 11169 (1996).

[224] P. E. Blöchl, Projector augmented-wave method, Phys. Rev. B **50**, 17953 (1994).

[225] G. Kresse and D. Joubert, From ultrasoft pseudopotentials to the projector augmented-wave method, Phys. Rev. B **59**, 1758 (1999).

[226] H. J. Monkhorst and J. D. Pack, Special points for Brillouin-zone integrations, Phys. Rev. B **13**, 5188 (1976).

[227] P. Canepa, Reducing self-interaction error in transition-metal oxides with different exact-exchange fractions for energy and density [Dataset], Zenodo (2025), https://doi.org/10.5281/zenodo.15741825.